Influence of a highly deformed surface layer on RCF predictions for rails in service

Wear 578–579 (2025) 206173

Contents lists available at ScienceDirect

Wear

journal homepage: www.elsevier.com/locate/wear

Influence of a highly deformed surface layer on RCF predictions for rails in service

Nasrin Talebi *, Björn Andersson, Magnus Ekh, Knut Andreas Meyer

Division of Material and Computational Mechanics, Department of Industrial and Materials Science, Chalmers University of Technology, SE-412 96 Gothenburg, Sweden

ARTICLE INFO

Keywords:
Anisotropy
Cyclic plasticity
Fatigue crack initiation
Rail profile change
Finite element simulations
Wheel passages

ABSTRACT

Rolling Contact Fatigue (RCF) cracks often initiate from the surface layer of rails, where large accumulated plastic deformations influence the mechanical and fatigue properties of the rail material. Additionally, changes in profile geometry due to both plasticity and wear result in alternating contact locations and conditions. The goal of this study is to investigate the importance of considering these effects when predicting surface RCF crack initiation in rails. We analyze their individual impact on stress and strain fields, as well as fatigue crack initiation, by finite element simulations of railheads subjected to a mixed traffic situation. To account for deformation-dependent material behavior, an anisotropic plasticity model is calibrated against experiments with different amounts of accumulated shear strains measured in field samples. Finally, a recently developed crack initiation criterion is employed that accounts for the influence of plastic deformations. Under extreme loading conditions, i.e., full slip with a traction coefficient of 0.4, it is shown that both deformed near-surface material and deformed geometry reduce the predicted RCF fatigue damage significantly, by factors of about 5 and 30, respectively. Furthermore, not accounting for the combined effect of deformed material state and geometry leads to approximately 150 times larger predictions of RCF damage.

1. Introduction

In the railway industry, RCF is a major source of problems in wheels and rails [1,2], reducing reliability and traffic safety [3]. Simulation tools that accurately predict RCF defects can improve reliability and safety by aiding maintenance planning and can provide a better understanding of the root causes of failures. However, the complex load scenarios and material behavior make such simulations challenging. High shear stresses due to traction and cornering forces within the small contact area between wheel and rail induce severe plastic deformations in the surface layer of rails and wheels [4,5]. These deformations accumulate over the service life, resulting in anisotropic behavior [6]. The highly deformed surface layer is known as the main region for the initiation of head checks, a common RCF defect [7,8]. In addition, the shape of rail and wheel profiles changes the contact conditions and contact stresses [9], which can consequently affect the resistance to fatigue crack initiation [10]. The present study aims to further enhance simulation accuracy by evaluating the importance of including the deformation-dependent material behavior and rail profile changes in RCF predictions.

To experimentally investigate the mechanical and fatigue properties of the deformed rail surface layer, techniques such as equal channel angular pressing [11], high-pressure-torsion [12,13], and predeformation [14] have been used in the literature. These studies show that the fatigue, fracture, and yield properties of rail steel change due to plastic deformations. Many models have been proposed to capture the evolution of anisotropic yield surfaces from an initially isotropic material state, often denoted as distortional hardening, see e.g. [15–18]. When evaluating the performance of a material in the deformed state, the yield surface is often characterized experimentally and modeled with a fixed anisotropy, see e.g. [19,20] for applications to sheet metal.

The performance of a railhead with a deformed surface layer under rolling contact conditions can be evaluated using models for the prediction of fatigue crack initiation. Plastic ratcheting-based models, purely energy-density based criteria, and approaches incorporating material microstructure into fatigue damage predictions represent some of the models and strategies developed in literature [21–24]. In addition, some studies adopt a critical plane search approach seeking for a plane with maximum fatigue damage [25–28]. For instance, in Pun et al. [27], the maximum Smith–Watson–Topper parameter (including the maximum normal stress and normal strain range [29]) on a critical plane was proposed as a single parameter to evaluate the initiation of macroscopic fatigue cracks in a railhead. Jiang and Sehitoglu [28]

* Corresponding author.
E-mail address: nasrin.talebi@chalmers.se (N. Talebi).

https://doi.org/10.1016/j.wear.2025.206173
Received 20 December 2024; Received in revised form 25 April 2025; Accepted 30 May 2025
Available online 16 June 2025

suggested a multiaxial Low Cycle Fatigue (LCF) criterion, in which normal stress, as well as shear stress and strain ranges on a given plane, contribute to the fatigue driving force in each loading cycle. This criterion considers the influence of compressive stresses on fatigue damage (which is found to be influential on the fatigue life of rail steels [30]), and it is appropriate for non-proportional loading. We extended this criterion in our previous paper [31], where the fatigue damage threshold was assumed to be dependent on the ratcheting strain.

Several studies have examined fatigue crack initiation in rails using Finite Element (FE) simulations of wheel–rail rolling contact conditions. Ringsberg [32] investigated the RCF crack initiation performance of a specific rail, using the recorded traffic loading in a three-dimensional (3D) FE model with an elastic–plastic material calibrated against uniaxial stress-controlled experiments and 3D moving contact distributions. In Pun et al. [33], the ratcheting performance of high strength rail steels was evaluated under rolling contact conditions, using a 3D FE model for a rail and a plasticity model calibrated against monotonic tensile tests, as well as uniaxial and biaxial cyclic loading experiments. A similar procedure was applied to evaluate the ratcheting performance of rails in curved tracks for higher axle loads [34]. Franklin et al. [35] developed a two-dimensional (2D) microstructural model (denoted the "brick" model) for simulating the accumulation of plastic shear strains during cyclic loading in the pearlitic microstructure. Ghodrati et al. [36] adopted a 3D FE model with crystal plasticity to simulate the material behavior in grains and used cohesive zone elements at the grain boundaries to study RCF crack initiation in wheel–rail rolling contact conditions. Trummer et al. [23] performed simulations of full-scale wheel–rail test rig experiments to investigate the propensity of fatigue crack initiation in the railhead using a model that accounts for large plastic deformations in the rail surface layer induced by wheel–rail contact. According to this model, the distribution of plastic shear strain in a crack initiation layer determines whether wear or a combination of wear and RCF crack initiation is the dominant damage mechanism. Additionally, they compared the distribution of the specific wear parameter (calculated as the $T\gamma$ parameter divided by the contact area) with the damage pattern observed in the test rig experiments. The empirical $T\gamma$ approach, which is based on the dissipated friction energy in the contact area, partially accounts for the interplay between wear and RCF crack initiation [37].

These fatigue performance investigations did not, however, account for the long-term accumulation of plastic deformations and its influence on the material behavior. This paper aims to study the effect of deformed near-surface material and deformed rail profile on stress and strain fields, as well as the accumulation rate of plasticity and fatigue damage in railheads under a loading sequence of mixed traffic. While acknowledging that the interaction between wear and macroscopic RCF crack initiation may influence the maximum fatigue damage results, the goal of this study is to provide insight into how different material states and profile geometry changes affect predictions of surface RCF crack initiation. To achieve this, the following procedure is adopted:

- We propose a distribution of large accumulated shear strains in a railhead based on measured shear strains in field samples (Section 2).
- A small-strain plasticity model accounting for an anisotropic yield surface is adopted. We identify the material parameters for different material states using multiaxial cyclic tests under non-proportional loading, together with pure axial and pure shear cyclic loading experiments, conducted after different levels of pre-deformation. Additionally, the predictive ability of the calibrated material model is evaluated (Section 3).
- For wheel over-rolling simulations, four railhead cases are considered, combining either initial or deformed material with initial or deformed geometry. Deformed material is accounted for by considering spatially varying material properties in the railhead. This variation is based on the distribution of accumulated shear strains. To model the rails under mixed traffic loading, a 2D FE-simulation setup is employed (Section 4).

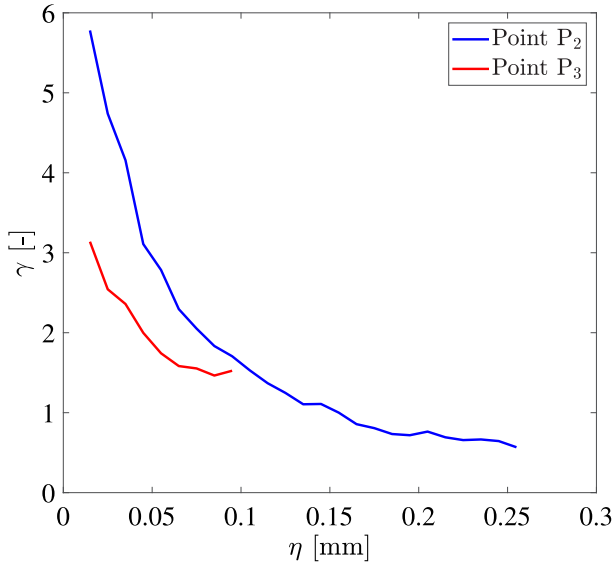

Fig. 1. Measured accumulated shear strains in rail samples (data from [30]).

- A recently developed crack initiation criterion accounting for plastic deformations is used to investigate how the deformed surface layer and geometry affect fatigue damage increment (Section 5).
- The results in terms of maximum von Mises stresses, as well as accumulated plasticity and fatigue damage during one loading sequence, are presented and discussed (Section 6).

2. Distribution of accumulated shear strains

Large shear strains accumulate heterogeneously in the railhead due to high wheel–rail contact stresses [4,5]. In this work, we reconstruct the distribution of these strains based on measured accumulated shear strains at the gauge corner and at the top of the rail from [30], corresponding to points P_2 and P_3 in Fig. 2. The rail samples were extracted from the main railway line in Sweden, between Stockholm and Gothenburg, after 11 and 14 years of mixed traffic loads. The dominant traffic on this line consists of passenger trains with axle loads between 15–19 tons, resulting in annual traffic of approximately $15 \cdot 10^6$ tons. Fig. 1 presents the measured accumulated shear strains γ at different depths η for points P_2 and P_3, excluding the first 10 μm due to high measurement uncertainties. A significant increase in γ can be observed close to the rail surface. Moreover, the measured values at the gauge corner (point P_2) are higher than those at the top of the rail (point P_3), up to a depth of approximately 0.1 mm. We obtain the distribution of accumulated shear strain over the railhead cross-section by interpolating the measured data, in the $\xi - \eta$ coordinate system, where ξ is the coordinate along the rail surface starting from point P_1, and η is the depth below the rail surface, see Fig. 2(a).

At points P_1 and P_4, the accumulated shear strains are assumed to be zero at all depths, and, in between, a linear interpolation scheme considering the measurements at points P_2 and P_3 is employed. Further, the depth of the anisotropic layer is assumed to be 0.5 mm, and outside this depth and also points P_1 and P_4 (based on typical contact regions), the material is considered isotropic. More details on how the closest point projection method is used to map a point in the railhead to the $\xi - \eta$ coordinate system, and how the distribution of γ is reconstructed, are given in Appendix A.

Fig. 2(a) illustrates the distribution of γ over the railhead cross-section. It indicates that γ decreases from the surface to the depth and

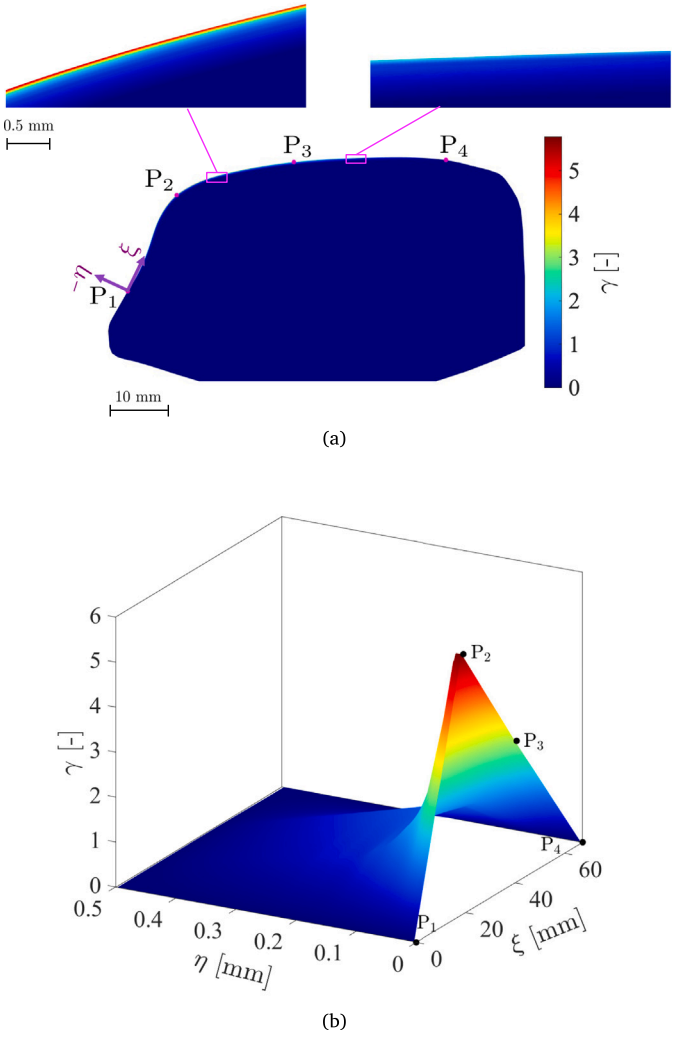

Fig. 2. (a) Assumed distribution of accumulated shear strain γ over the railhead cross-section, and (b) shear strain γ versus ξ and η.

also varies in the transverse direction, which is in accordance with the measurements. This variation is further detailed in Fig. 2(b). At $\eta = 0$, the shear strain increases up to the gauge corner of the rail before dropping to zero at point P_4. Furthermore, there is a significant shear strain gradient in the first 0.1 mm below the rail surface, followed by a more gradual decrease in γ with increasing depth η. Note that the same distribution of γ has been considered in the fictitious case of railhead with initial geometry and deformed material. The purpose of considering the fictitious case is to study the individual influence of the deformed material. For the wheel over-rolling simulations, described in Section 4, we will use the distribution of γ to define anisotropy in the FE model of the railhead cross-section. Additionally, fatigue crack initiation will be affected by the γ-dependent initial ratcheting strains, see Section 5.

3. Material modeling and calibration

In this section, the adopted plasticity model is explained first. Subsequently, the considered experiments for the calibration of the material model and the parameter identification procedure are elaborated.

3.1. Material model formulation

In the present study, we adopt a small-strain cyclic plasticity model with an anisotropic yield surface, based on the finite strain material model formulation developed by Meyer and Menzel [38]. First, the notations used for describing the material model are presented. Second-order tensors are written in boldface, e.g. $\boldsymbol{t}$, while fourth-order tensors are written in capitalized, boldface, and upright form, e.g. $\mathbf{T}$. The non-standard open product $\overline{\otimes}$ between two second-order tensors is defined as: $\boldsymbol{a} \,\overline{\otimes}\, \boldsymbol{b} = a_{ik}\, b_{jl}\, \boldsymbol{e}_i \otimes \boldsymbol{e}_j \otimes \boldsymbol{e}_k \otimes \boldsymbol{e}_l$. $\boldsymbol{I}$ is the second-order identity tensor, and the fourth-order deviatoric identity tensor is $\mathbf{I}^{\mathrm{dev}} = \boldsymbol{I} \,\overline{\otimes}\, \boldsymbol{I} - \boldsymbol{I} \otimes \boldsymbol{I}/3$.

The total strain, $\boldsymbol{\epsilon}$, is additively decomposed into an elastic, $\boldsymbol{\epsilon}^{\mathrm{e}}$, and a plastic, $\boldsymbol{\epsilon}^{\mathrm{p}}$, strain

$$\boldsymbol{\epsilon} = \boldsymbol{\epsilon}^{\mathrm{e}} + \boldsymbol{\epsilon}^{\mathrm{p}} \tag{1}$$

Linear isotropic elasticity is assumed

$$\boldsymbol{\sigma} = \mathbf{E}^{\mathrm{e}} : \boldsymbol{\epsilon}^{\mathrm{e}} \quad \text{where} \quad \mathbf{E}^{\mathrm{e}} = 2\,G\,\mathbf{I}^{\mathrm{dev}} + K_{\mathrm{b}}\,\boldsymbol{I} \otimes \boldsymbol{I}, \quad K_{\mathrm{b}} = \frac{E\,G}{3\,(3\,G - E)} \tag{2}$$

where G, K_{b}, and E are the shear, bulk, and Young's moduli, respectively. The anisotropic yield function of Hill type is formulated as

$$\boldsymbol{\Phi} = \sqrt{\boldsymbol{\sigma}_{\mathrm{red}}^{\mathrm{dev}} : \hat{\mathbf{C}} : \boldsymbol{\sigma}_{\mathrm{red}}^{\mathrm{dev}}} - Y \leq 0 \quad \text{with} \quad \boldsymbol{\sigma}_{\mathrm{red}}^{\mathrm{dev}} = \boldsymbol{\sigma}^{\mathrm{dev}} - \sum_{i=1}^{N_{\mathrm{back}}} \boldsymbol{\beta}_i \tag{3}$$

where $\boldsymbol{\sigma}_{\mathrm{red}}^{\mathrm{dev}}$ is the reduced deviatoric stress, $\hat{\mathbf{C}}$ is the fourth-order anisotropy tensor, Y is the isotropic hardening, and $\boldsymbol{\beta}_i$ are the back-stresses. Two back-stresses ($N_{\mathrm{back}} = 2$) are considered in this study. We assume that the anisotropy tensor does not evolve from the initial state described by the accumulated shear strain γ defined in Section 2, see Section 3.5 for more details.

The evolution of the plastic strain, $\boldsymbol{\epsilon}^{\mathrm{p}}$, is considered to be of associative type

$$\dot{\boldsymbol{\epsilon}}^{\mathrm{p}} = \dot{\lambda}\,\frac{\partial \boldsymbol{\Phi}}{\partial \boldsymbol{\sigma}} = \dot{\lambda}\,\boldsymbol{\nu} \quad \text{with} \quad \boldsymbol{\nu} = \frac{1}{2\sqrt{\boldsymbol{\sigma}_{\mathrm{red}}^{\mathrm{dev}} : \hat{\mathbf{C}} : \boldsymbol{\sigma}_{\mathrm{red}}^{\mathrm{dev}}}}\left[\hat{\mathbf{C}} : \boldsymbol{\sigma}_{\mathrm{red}}^{\mathrm{dev}} + \boldsymbol{\sigma}_{\mathrm{red}}^{\mathrm{dev}} : \hat{\mathbf{C}}\right] \tag{4}$$

where $\dot{\lambda}$ is the plastic multiplier (rate of the accumulated equivalent plastic strain) and can be determined from the Karush–Kuhn–Tucker loading/unloading conditions

$$\boldsymbol{\Phi} \leq 0, \quad \dot{\lambda} \geq 0, \quad \boldsymbol{\Phi}\,\dot{\lambda} = 0 \tag{5}$$

The evolution law for the isotropic hardening is chosen to be of Voce-type and is formulated as

$$Y = Y_0 + \sum_{i=1}^{2} Y_{\infty,i}\left[1 - \exp\left(-\kappa_{\mathrm{iso},i}\,\lambda\right)\right], \quad \lambda = \int_0^t \dot{\lambda}\,\mathrm{d}t \tag{6}$$

with the initial yield stress Y_0. $Y_{\infty,i}$ and $\kappa_{\mathrm{iso},i}$ control the saturation of isotropic hardening and the hardening rates, respectively. The evolution of kinematic hardening follows the non-associative combined Armstrong–Frederick [39] and Burlet–Cailleteuad [40] law, which was first proposed by Delobelle et al. [41]

$$\dot{\boldsymbol{\beta}}_i = -\frac{2}{3}\,H_{\mathrm{kin},i}\,\dot{\lambda}\left[-\boldsymbol{\nu} + \boldsymbol{\nu} : \boldsymbol{\nu}\;\delta\,\frac{\boldsymbol{\beta}_i}{\beta_{\infty,i}} + (1-\delta)\,\frac{\boldsymbol{\beta}_i : \boldsymbol{\nu}}{\beta_{\infty,i}}\,\boldsymbol{\nu}\right] \tag{7}$$

where $H_{\mathrm{kin},i}$ are kinematic hardening moduli, the material parameter δ controls the amount of Armstrong–Frederick versus Burlet–Cailletaud type of kinematic hardening, and $\beta_{\infty,i}$ are the saturation values of the back-stresses.

3.2. Experiments for material model calibration and validation

To obtain similar material states to those found in the surface layer of in-service rails, an experimental method was developed by Meyer et al. [30]. The details of the experimental technique have been explained in [30], and the setup is briefly described here. Solid cylindrical test bars, extracted from railheads with virgin pearlitic R260 steel, were used for predeformation, with the dimensions shown in Fig. 3(a) (top). They were twisted in increments of 90° under constant

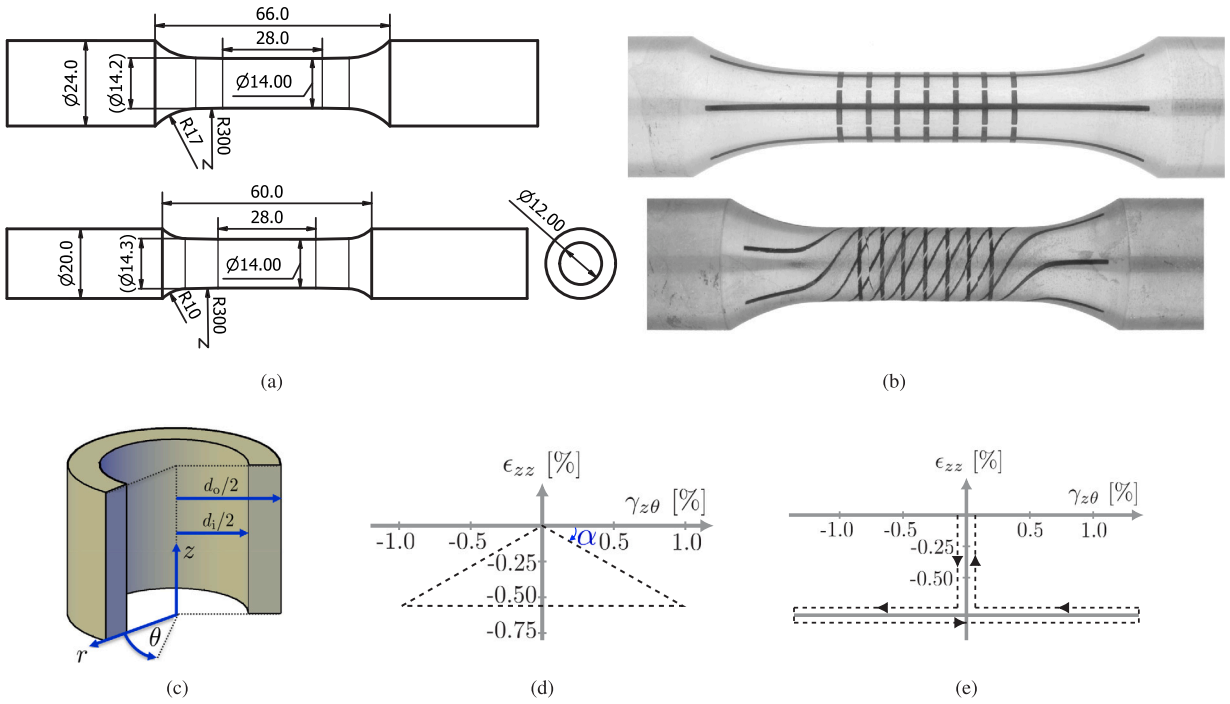

Fig. 3. (a) Dimensions of solid (top) and tubular (bottom) test bars in mm [14], (b) undeformed (top) and predeformed (bottom) solid test bars [30], (c) cylindrical coordinate system and dimensions for the thin-walled tubular test bars, and loading paths for non-proportional multiaxial cyclic tests with (d) 0.80% and (e) 1.12% von Mises strain amplitudes.

Table 1
Identified elastic parameters and initial back-stress components for each predeformation level. PD_x denotes x cycles of predeformation.

PD_x	E	G	$\beta^0_{1,zz}$	$\beta^0_{1,z\theta}$
PD_0	192.8	74.9	−4.8	−6.0
PD_1	194.3	76.3	−72.1	−109.4
PD_3	194.1	72.3	−73.4	−105.4
PD_6	195.7	69.4	−49.0	−96.2
Unit	GPa	GPa	MPa	MPa

compressive stress of −600 MPa, and, subsequently, both the torque and axial force were relaxed. In addition to the undeformed case, 1, 3, and 6 cycles of predeformation were investigated, resulting in surface shear strains of 0.21, 0.60, and 1.13, respectively. These are denoted as PD_0, PD_1, PD_3, and PD_6 in the following.

Fig. 3(b) shows the solid test bars marked with laser-etched grids to visualize the surface shear strains before and after predeformation. To minimize the influence of the radially varying shear strain, the test bars were remachined to form thin-walled tubular shapes with inner diameter $d_i = 12$ mm and outer diameter $d_o = 14$, see Fig. 3(a) (bottom) and [14].

After remachining, the undeformed and predeformed tubular test bars were subjected to pure axial, pure shear, or non-proportional multiaxial cyclic loading with a 0.80% or 1.12% von Mises strain amplitude (ϵ^a_{vM}) on the surfaces of the test bars, in different loading directions in $\epsilon_{zz} - \gamma_{z\theta}$ plane, see Fig. 3(c) for the definition of the coordinate system. The results from the pure axial or shear tests are used to determine the elastic material parameters, E and G, as well as the initial back-stress components, $\beta^0_{1,zz}$ and $\beta^0_{1,z\theta}$, for each predeformation level. Note that, we have assumed that only the first back-stress is influenced by the predeformation and that $\beta^0_{1,rr} = \beta^0_{1,\theta\theta} = -0.5\,\beta^0_{1,zz}$, since $\boldsymbol{\beta}^0_1$ is deviatoric. The identified parameters and initial back-stress components are presented in Table 1.

The considered loading path in the experiments under non-proportional loading with $\epsilon^a_{vM} = 0.80\%$ is shown in Fig. 3(d). Each cycle of the strain-controlled experiments starts with compressive normal strain ϵ_{zz} and shear strain $\gamma_{z\theta}$ applied in a loading direction defined by the angle α: 45.0°, 67.5°, 112.5°, and 135.0°. After reaching a magnitude of 0.56%, ϵ_{zz} is maintained constant, while $\gamma_{z\theta}$ gradually changes to the same magnitude but reversed direction. The loading cycle ends with the simultaneous unloading of ϵ_{zz} and $\gamma_{z\theta}$. These experiments provide data for calibration of the adopted plasticity model, see Section 3.3. The number of experiments included in the calibration procedure is 1 for PD_0 and 3 for PD_1 to PD_6. The number of cycles of the non-proportional loading tests is shown in Table 2, and it was chosen to ensure that fatigue damage (i.e., softening) had not yet affected the stress amplitudes. These experiments, which involve pulsating compression and alternating shear, aim to subject the predeformed test bars to loading conditions similar to those experienced by rail material during wheel–rail rolling contact.

Fig. 3(e) shows the loading path used in the non-proportional loading experiments with $\epsilon^a_{vM} = 1.12\%$. In these tests, ϵ_{zz} is first applied up to a magnitude of 0.8%, after which it is held constant, while $\gamma_{z\theta}$ is introduced. Once $\gamma_{z\theta}$ reaches a magnitude of 1.36%, it reverses to an equal magnitude in the opposite direction. Finally, both ϵ_{zz} and $\gamma_{z\theta}$ are reduced to zero at the end of the loading cycle. These experiments are used as validation data to assess the predictive ability of the adopted plasticity model. This procedure includes 1 experiment for PD_0 and 1 for PD_6.

The only non-zero stress components are assumed to be σ_{zz} and $\sigma_{z\theta}$. The mean values of the stresses over the wall thickness, $\bar{\sigma}_{zz}$ and $\bar{\sigma}_{z\theta}$, are computed as in [14]

$$\bar{\sigma}_{zz} = \frac{4\,F_a}{\pi\left(d_o^2 - d_i^2\right)} \tag{8}$$

$$\bar{\sigma}_{z\theta} = \frac{16\,T}{\pi\left(d_o^2 - d_i^2\right)\left(d_o + d_i\right)} \tag{9}$$

where F_a and T are the applied axial force and torque, and d_o, as well as d_i, are shown in Fig. 3(c). The rotation φ over the gauge length L_g=12 mm and the axial strain ϵ_{zz} were measured by an extensometer [14]. It is assumed that the shear strains ϵ_{rz} and $\epsilon_{r\theta}$ are zero, and the mean shear strain over the wall thickness is computed as

$$\gamma = 2\bar{\epsilon}_{z\theta} = \frac{\varphi\left(d_o + d_i\right)}{4\,L_g} \tag{10}$$

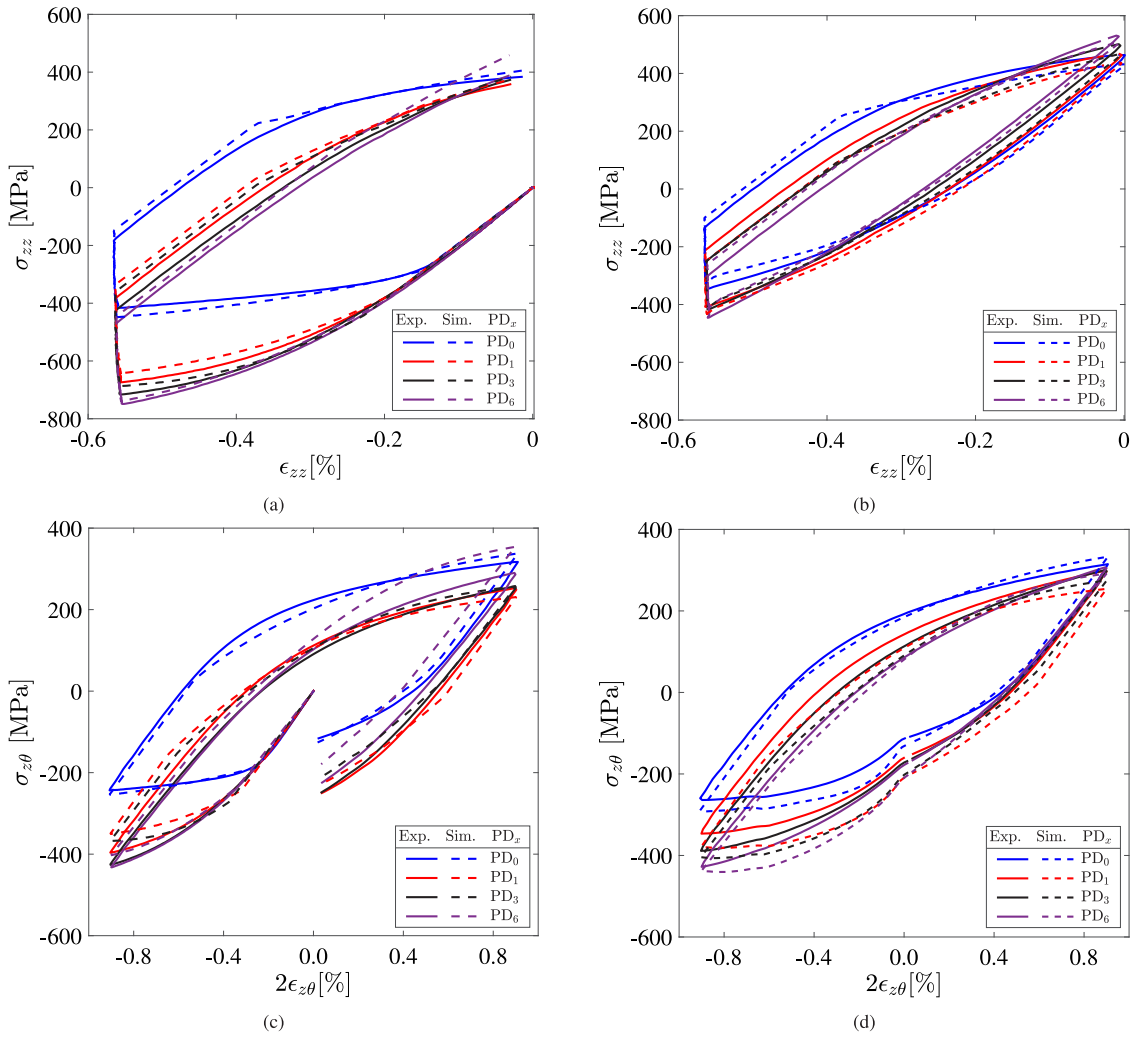

Fig. 4. Calibrated stress–strain response for the axial direction: (a) cycle 1 and (b) cycle 100, and for the shear direction: (c) cycle 1 and (d) cycle 100. The experiments were performed with $\epsilon^{a}_{vM} = 0.80\%$. Exp. and Sim. denote the experimental and simulation results, respectively. The loading angle, α, is 135°, and PD$_x$ refers to x cycles of predeformation.

Table 2
Information about the non-proportional multiaxial cyclic loading tests with $\epsilon^{a}_{vM} = 0.80\%$. PD$_x$ denotes x cycles of predeformation.

PD$_x$	Loading angle, α [°]	N_f
PD$_0$	135.0	1021
PD$_1$	45.0	900
PD$_1$	112.5	2108
PD$_1$	135.0	1250
PD$_3$	45.0	915
PD$_3$	112.5	660
PD$_3$	135.0	669
PD$_6$	67.5	871
PD$_6$	112.5	1055
PD$_6$	135.0	722

Some results from the non-proportional loading experiments are illustrated in Figs. 4(a)–4(d) and 5(a)–5(d). In Figs. 4(a) and 4(c), both axial and shear responses in cycle 1 show that higher levels of predeformation result in an increase in the hardening slope, which is particularly noticeable when comparing PD$_0$ and PD$_1$. However, the effect diminishes with more predeformation. After one loading cycle, the residual normal stresses become similar, while the difference in the shear stress between predeformation levels remains more pronounced. A similar trend can be observed when considering the axial and shear responses in cycle 100 in Figs. 4(b) and 4(d), although the differences between predeformation levels are less noticeable. Moreover, material softening becomes apparent after 100 cycles, especially in the axial response of the predeformed cases, see Fig. 4(b). Similar trends are observed in the experiments under non-proportional loading with $\epsilon^{a}_{vM} = 1.12\%$ (Figs. 5(a)–5(d)).

3.3. Material model calibration

This section presents the procedure to identify the remaining 10 material parameters of the adopted plasticity model for each predeformation level based on the cyclic non-proportional multiaxial experiments with $\epsilon^{a}_{vM} = 0.80\%$ (Fig. 3(d)). The objective function for each predeformation level that we minimize using the gradient-free, Nelder–Mead simplex algorithm [42], employing matmodfit [43,44], is formulated as

$$E_{obj} = \sum_{k=1}^{N_{exp}} E_{k,obj} \quad \text{with} \quad E_{k,obj} = \sum_{i=1}^{N} \frac{1}{t_{end} - t_{start}} \sum_{j=1}^{M} \left(S^{i}_{sim}(t_j) - S^{i}_{exp}(t_j) \right)^2 \Delta t_j \tag{11}$$

where $E_{k,obj}$ is the objective function for each experiment k, $S^{i}_{exp}(t_j)$ and $S^{i}_{sim}(t_j)$ are the stress values from the experiments and simulations at time step t_j, M is the total number of time steps, and N is the number of measurement channels (here $N = 2$ for axial and torsional channels).

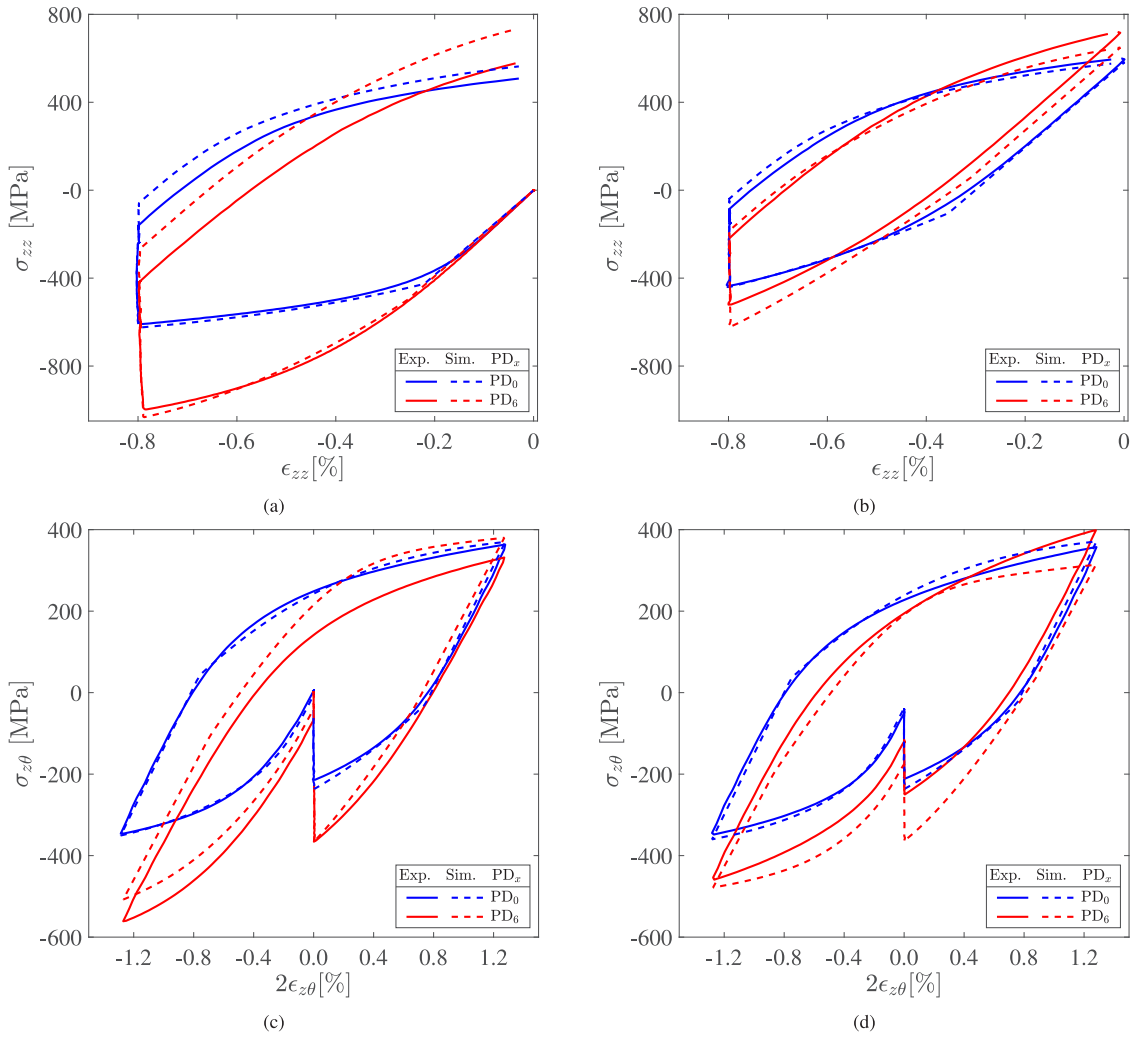

Fig. 5. Validation of the stress–strain response for the axial direction: (a) cycle 1 and (b) cycle 100, and for the shear direction: (c) cycle 1 and (d) cycle 100. The experiments were performed with $\epsilon^{a}_{vM} = 1.12\%$. Exp. and Sim. denote the experimental and simulation results, respectively. PD$_x$ refers to x cycles of predeformation.

We use a step-wise calibration approach. It starts by considering only the first 30 loading cycles. Among 200 initial guesses generated by the Latin Hypercube sampling method, 50 parameter sets with the lowest E_{obj} are selected as initial guesses for the optimizer, and the 20 optimized parameter sets with the lowest E_{obj} are selected as initial guesses in the second step. 50 loading cycles are considered in the second step of optimization, and the 10 best-optimized parameter sets are passed to the next step. In the third step, these 10 parameter sets are used as initial guesses when considering 500 loading cycles, and then, the 8 parameter sets with the lowest E_{obj} are selected. These 8 parameter sets are used as initial guesses in the final step, where all loading cycles are included in the optimization procedure, and the parameter set with the lowest E_{obj} is finally selected. The identified parameters are listed in Table 3 for each level of predeformation. The goal of this step-wise calibration approach has been to find a global optimum for each predeformation level, but, due to the non-convex objective function, it cannot be guaranteed. The identified material parameters for each predeformation level will be used in Section 4 in order to consider the deformed surface layer in the railhead, whose material properties vary with spatial position.

By examining the experimental and calibrated simulation results in Figs. 4(a) and 4(c) for cycle 1, it can be seen that the experimentally observed larger hardening for higher predeformation levels is captured by the material model. The difference between the residual normal stresses in the simulations across different predeformation levels is larger compared to those in the experiments in contrast to the residual shear stresses. Considering the simulated axial response in cycle 100, the maximum σ_{zz} for all predeformation levels is slightly underestimated. This is more apparent in the shear response. Despite the differences, the overall agreement between the experiments and simulations is reasonable, considering the complexity of the experimental loading (non-proportional multiaxial loading) and the inclusion of many loading cycles in the optimization procedure.

Table 3
Identified material model parameters for each predeformation level. PD$_x$ denotes x cycles of predeformation.

PD$_x$	Y_0	$k_{iso,1}$	$Y_{\infty,1}$	$k_{iso,2}$	$Y_{\infty,2}$	δ	$H_{kin,1}$	$\beta_{\infty,1}$	$H_{kin,2}$	$\beta_{\infty,2}$
PD$_0$	419	600	−120	981	45	0.88	3.2	19	104	0.32
PD$_1$	435	446	−451	468	372	0.54	13.0	69	231	0.43
PD$_3$	559	681	−516	1293	298	0.64	6.7	43	272	0.53
PD$_6$	501	22	−225	382	57	0.67	12.9	1374	414	0.55
Unit	MPa	–	MPa	–	MPa	–	GPa	GPa	GPa	GPa

3.4. Material model validation

After the calibration of the material parameters explained in Section 3.3, we use the identified material parameters in order to predict the stress–strain response of the multiaxial non-proportional cyclic tests with $\epsilon^{a}_{vM} = 1.12\%$, see Fig. 3(e) in Section 3.2. The predicted shear and

axial stress–strain responses for cycles 1 and 100 are shown in Fig. 5. The overall stress–strain behavior for both PD_0 and PD_6 has been predicted by the calibrated plasticity model, with a closer agreement to the experimental results for the undeformed material (PD_0) than for the material predeformed by 6 cycles (PD_6). Considering the fact that ϵ^{a}_{vM} in these data is different from that in the calibration data, the predicted axial and shear stress–strain responses for both predeformation levels are reasonable.

3.5. FE simulations of predeformation tests

As stated in Section 3.1, in the present paper, we assume that there is no evolution of anisotropy from its initial state, during the non-proportional multiaxial cyclic tests (see Section 3.2) and during the over-rolling simulations (see Section 4). We perform FE simulations of the predeformation tests to obtain the initial anisotropy tensors, $\hat{\mathbf{C}}$, for different predeformation levels. The simulations are conducted in the commercial FE code Abaqus [45] using 8-node quadratic axisymmetric elements with reduced integration and additional degrees of freedom for twist (referred to as CGAX8R in Abaqus). The finite strain material model formulation from Meyer and Menzel [38] with the model parameters from [31] is used in these simulations. It uses the yield criterion

$$\Phi_{\mathrm{M}} = \sqrt{\left[\boldsymbol{M} - \boldsymbol{M}_{\mathrm{k}}\right] : \hat{\mathbf{C}}_{\mathrm{M}} : \left[\boldsymbol{M} - \boldsymbol{M}_{\mathrm{k}}\right]} - Y \tag{12}$$

where $\boldsymbol{M}$ and $\boldsymbol{M}_{\mathrm{k}}$ are the Mandel stress and the sum of the back-stresses, respectively. The Mandel stress is defined as $\boldsymbol{M} = \det(\boldsymbol{F})\left[\boldsymbol{F}^{\mathrm{e}}\right]^{\mathrm{T}}\boldsymbol{\sigma}\left[\boldsymbol{F}^{\mathrm{e}}\right]^{-\mathrm{T}}$, where $\boldsymbol{F}$ and $\boldsymbol{F}^{\mathrm{e}}$ are the deformation gradient and the elastic deformation gradient. Due to plastic incompressibility, $\det(\boldsymbol{F}) \approx 1$, and we obtain the equivalent anisotropy tensor $\hat{\mathbf{C}}$ on the current configuration as

$$\hat{\mathbf{C}} = \left[\left[\boldsymbol{F}^{\mathrm{e}}\right] \overline{\otimes} \left[\boldsymbol{F}^{\mathrm{e}}\right]^{-\mathrm{T}}\right] : \hat{\mathbf{C}}_{\mathrm{M}} : \left[\left[\boldsymbol{F}^{\mathrm{e}}\right]^{\mathrm{T}} \overline{\otimes} \left[\boldsymbol{F}^{\mathrm{e}}\right]^{-1}\right] \tag{13}$$

which is used in Eq. (3).

The anisotropy tensor, $\hat{\mathbf{C}}_{\mathrm{M}}$, is extracted for PD_1, PD_3, and PD_6, at the locations where the test data during the cyclic tests were collected. Specifically, using the mesh size 0.3 mm, the results have been extracted at $r = 6.52$ mm and $z = 0.07$ mm for the PD_1 tests, at $r = 6.57$ mm and $z = 0.07$ mm for the PD_3 tests, and at $r = 6.52$ mm and $z = 0.06$ mm for the PD_6 tests, respectively. More details of the material model for the FE simulations of the predeformation tests and its parameter values can be found in Meyer and Menzel [38] and Talebi et al. [31].

4. Over-rolling simulations

In this section, we discuss how the deformed material is introduced into an FE model of a railhead, how the FE model is defined, and what traffic loading the FE model is subjected to.

4.1. Anisotropy in railhead cross-section

We introduce predeformation in the railhead cross-section using the anisotropy tensors, $\hat{\mathbf{C}}$, and the identified material parameters for different predeformation levels (see Tables 1 and 3), characterized by certain amounts of surface shear strain, together with the distribution of accumulated shear strains (see Section 2). Thereby, for a given γ at an integration point in the railhead cross-section, the material parameters and anisotropy tensor have been determined using linear interpolation between the values from PD_0 to PD_6. Furthermore, if γ exceeds 1.13, corresponding to PD_6, the parameters are set to those of PD_6. Note that, the components of the initial back-stress, $\boldsymbol{\beta}^0_1$, and the anisotropy tensor, $\hat{\mathbf{C}}$, need to be transformed from the local coordinate system $\xi - \eta$ to the global coordinate system $x - y$, see Fig. 6. This is done using the angle θ and the coordinate transformation matrix $\underline{Q}$

$$\underline{Q} = \begin{bmatrix} \cos(\theta) & \sin(\theta) & 0 \\ \sin(\theta) & -\cos(\theta) & 0 \\ 0 & 0 & -1 \end{bmatrix} \tag{14}$$

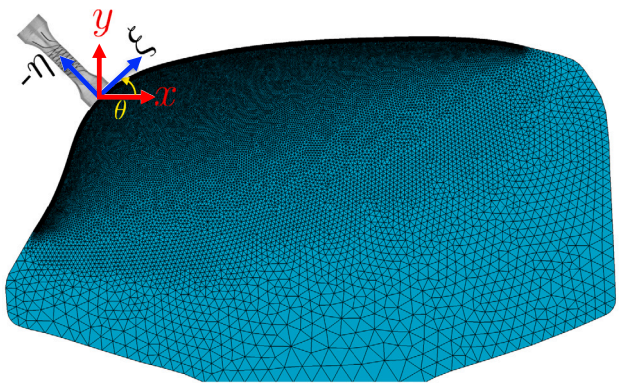

Fig. 6. Schematic illustration of coordinate transformation in the railhead cross-section.

By using index notations, the transformations can be written as

$$\left[\boldsymbol{\beta}^0_1\right]_{ij} = \underline{Q}^{\mathrm{T}}_{ik'}\,\left[\boldsymbol{\beta}^0_1\right]_{k'l'}\,\underline{Q}_{l'j} \quad \text{and} \quad \left[\hat{\mathbf{C}}\right]_{ijkl} = \underline{Q}^{\mathrm{T}}_{im'}\,\underline{Q}^{\mathrm{T}}_{jn'}\left[\hat{\mathbf{C}}\right]_{m'n'o'p'}\,\underline{Q}_{o'k}\,\underline{Q}_{p'l} \tag{15}$$

where $\left[\boldsymbol{\beta}^0_1\right]_{k'l'}$ and $\left[\hat{\mathbf{C}}\right]_{m'n'o'p'}$ are the components in the $\xi - \eta$ coordinate system, whereas $\left[\boldsymbol{\beta}^0_1\right]_{ij}$ and $\left[\hat{\mathbf{C}}\right]_{ijkl}$ are the components in the $x - y$ coordinate system.

4.2. Rail finite element model

To capture the gradients in the material properties near the rail surface, a very fine mesh is required. Therefore, to have a computationally efficient FE-simulation setup for modeling the rail during train wheel over-rollings, a 2D Generalized Plane Strain (GPS) model developed by Andersson et al. [46] is employed. The simulation methodology is explained in detail in [46] and is briefly described below. Moreover, these FE simulations are conducted in the commercial software Abaqus [45] using 6-node quadratic triangular GPS elements, referred to as CPEG6 in Abaqus. Further details regarding the generalized plane strain elements can be found in the Abaqus theory manual [45], Section "Generalized plane strain elements". The 50E3 rail profile is used in accordance with the measurements of the accumulated shear strains, see Section 2.

In the implementation of the 2D GPS model, the 2D cross-section has a constant curvature with respect to the out-of-plane direction and lies between two rigid bounding planes, as illustrated in Fig. 7(a). These planes are capable of translating axially (Δz) and rotating around the x- and y-axes ($\Delta\alpha, \Delta\beta$, respectively) relative to each other about a predefined pivot point in the plane (x_0, y_0). Hence, the displacement in the z direction can be written as

$$u_z(x, y) = \Delta z + \Delta\alpha\,(y - y_0) - \Delta\beta\,(x - x_0) \tag{16}$$

Consequently, the normal strain in the z-direction, which can be described as the strain in a curved out-of-plane element fiber between the two bounding planes, varies linearly with respect to the in-plane position, cf. [45]. Furthermore, the out-of-plane bending and axial stiffnesses of the rail are accounted for by assigning axial and bending stiffnesses to the translational and rotational degrees of freedom of the bounding planes. The out-of-plane stiffnesses are tuned to match those of a full-scale 3D FE model and have also been validated against a bar and the Euler–Bernoulli beam model.

In order for the 2D over-rolling simulation to replicate a Hertzian contact pressure distribution traversing longitudinally on the rail surface in a 3D space, the element thicknesses of the 2D GPS model have been scaled [47]. This scaling is tuned such that the variation of the maximum von Mises for each over-rolling, plotted along a stress

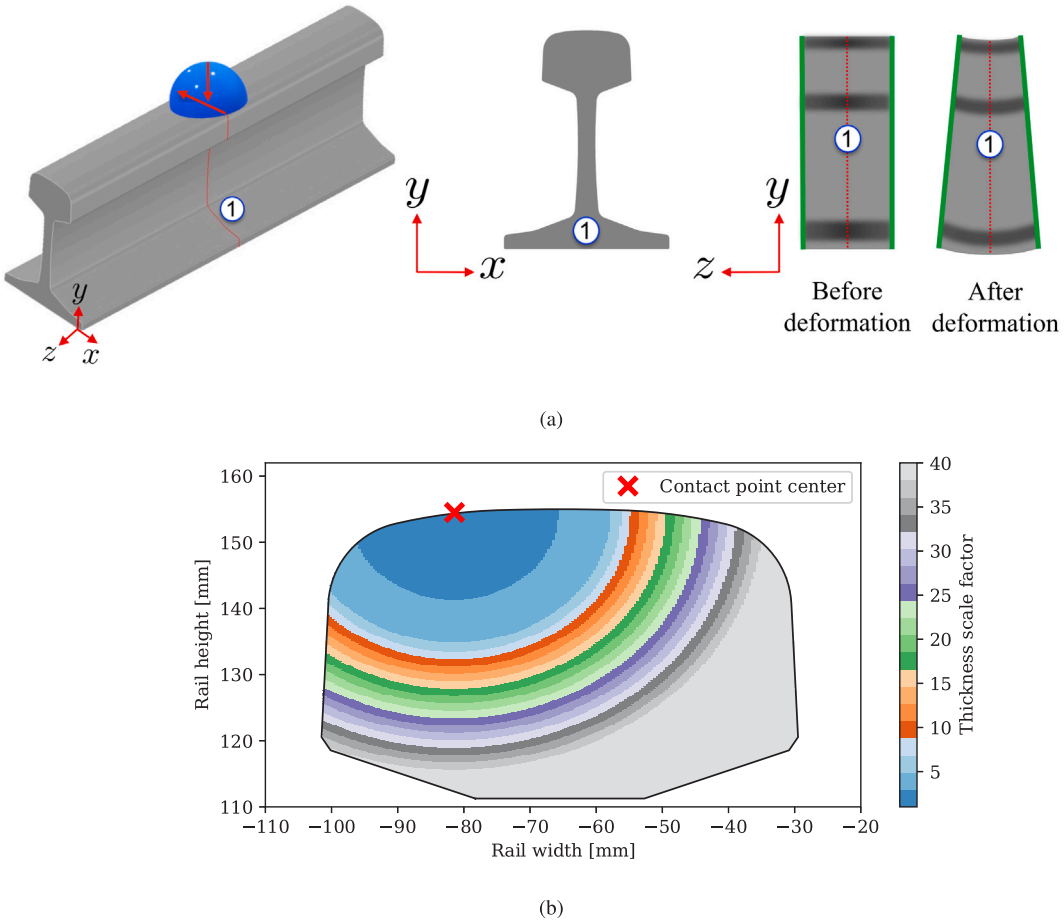

(a)

(b)

Fig. 7. (a) Schematic illustration of the 2D GPS model assumptions. The green lines are rigid bounding planes surrounding the rail cross-section. (b) FE element thickness scaling factors in the 2D GPS model following [47]. (For interpretation of the references to color in this figure legend, the reader is referred to the web version of this article.)

path from the center of the rail foot to the contact position in the 2D GPS model, mimics that of the 3D model. In this procedure, a piecewise linear scaling profile of the thicknesses of FE elements is used, with the scaling factor being a function of the distance from the element integration point to the center of the Hertzian contact pressure distribution. The element thickness scaling factors for the railhead with initial geometry are illustrated in Fig. 7(b) using the load parameters from the first wheel over-rolling. The scaling procedure is further described in C. It should be noted that only transverse traction can be applied to the rail FE model.

It has been demonstrated that the 2D GPS model can reproduce the results of the full-scale 3D model with good accuracy and a noticeable reduction in the computational time [46]. Based on [47], we have computed that the maximum computational error in the longitudinal (out-of-plane) stress component is less than 10% and that the computational time is reduced to approximately 5% of the 3D model's runtime. The material model presented in Section 3.1, which uses the implicit backward Euler time discretization scheme, together with the scaling factor function, is implemented as a user-defined subroutine in Abaqus, and the FE models are generated using Python scripts through the Abaqus scripting interface [45].

4.3. Representative traffic load sequence

The over-rolling simulation setup that we adopt in this study uses some parts of the iterative simulation methodology proposed by Skrypnyk et al. [48] to predict the long-term evolution of the rail profile. In short, the methodology starts from multibody dynamics simulations, providing information about the contact positions and wheel–rail contact forces. Subsequently, the contact patch sizes and maximum contact pressure are computed based on the Hertzian-based metamodel developed by Skrypnyk et al. [49], which accounts for plasticity in the rail material. We use the simulation methodology and traffic situation from Ansin et al. [50] on 50E3 rail profiles with initial and deformed geometries. The load sequence consists of 348 wheel passages, based on the traffic situations in a circular curve with a radius of 1974 m, located at the west mainline in Sweden between Nyckelsjön and Sparreholmen. The contact positions and wheel–rail contact forces, obtained from the multibody dynamics simulations, are extracted from the high rail, as the gauge corner of a high rail is the region of interest for the initiation of head checks, cf. [2]. For the railhead with initial geometry, 32 wheel passages have 2-point contact, and 10 cases have excessive contact patch sizes, resulting in 370 considered contact loadings. The corresponding numbers for the deformed geometry are 63 cases of 2-point contact and 24 cases of excessive contact patch sizes, resulting in 387 contact loadings. The reason for not considering the contact loadings with excessive contact patch sizes is that they gave unrealistic contact loading locations (outside the cross-section), and that they do not make a significant contribution to the plastic deformations. The load sequence represents the variation of passenger vehicles (with axle loads ranging from 11.7 to 21.0 tonnes), wheel profiles (279 different measured geometries), and vehicle speeds. The rail material at the measurement location was steel grade R260 [50].

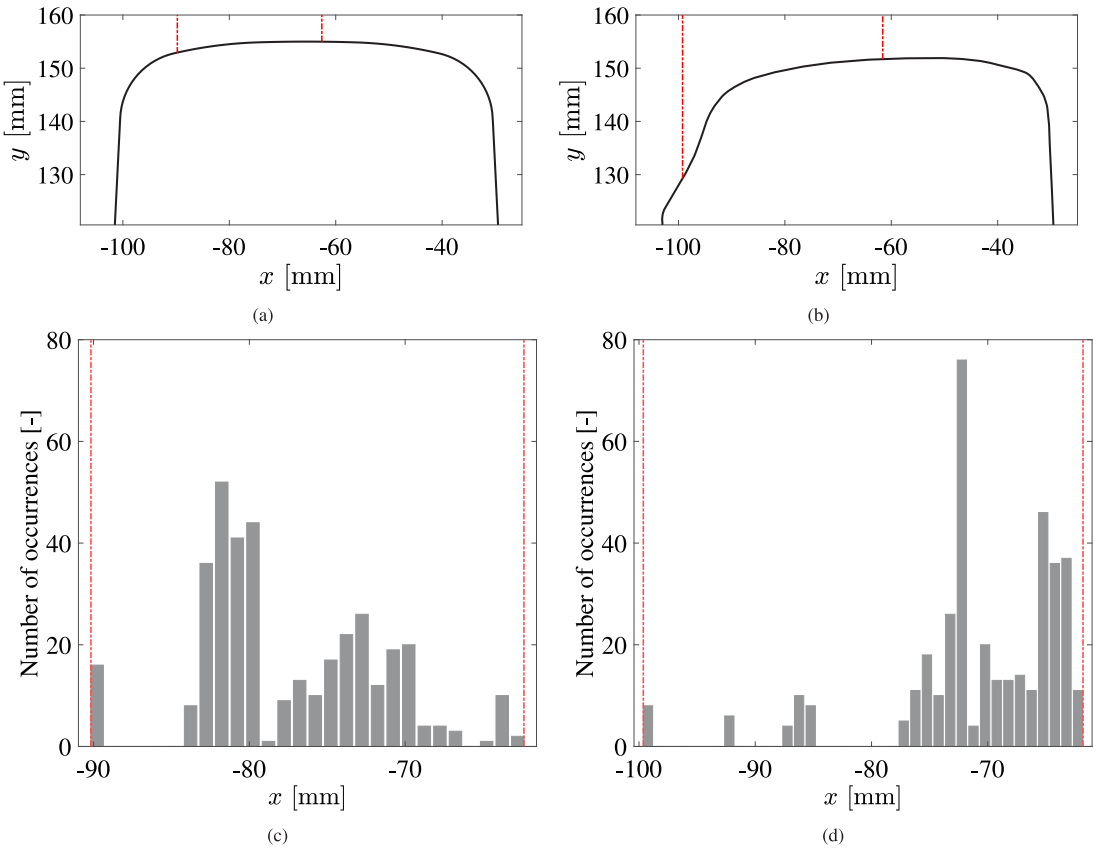

Fig. 8. Railhead geometry for the 50E3 rail profile with the (a) initial and (b) deformed geometries, along with the corresponding distribution of contact points in the railheads with the (c) initial and (d) deformed geometries. The region between the red dashed lines in each sub-figure denotes the contact zones. The reader is referred to Fig. 7(a) for the location of the coordinate system in the rail cross-section.

Fig. 8 shows the range of contact positions on the railheads for both the initial and deformed geometries, as well as their number of occurrences. For the initial geometry, wheel–rail contacts most often occur within a narrow 3 mm band, ranging from −83 mm to −80 mm. For the geometrically deformed railhead, the majority of contacts are distributed between −71 mm and -62 mm. This paper assumes full slip condition with a traction coefficient of 0.4, resulting in proportional traction distribution relative to contact pressure distribution. The resulting stresses, accumulated plasticity, and fatigue damage after one load sequence applied to the rail FE model will be presented and discussed in Section 6.

5. Fatigue crack initiation criterion

In order to investigate the effect of deformed material and geometry on the fatigue performance of a railhead subjected to traffic loading, we apply a recently developed crack initiation criterion, see Talebi et al. [31]. The criterion is a modified version of the multiaxial low cycle fatigue criterion proposed by Jiang and Sehitoglu [28], which is based on the critical plane search approach. On a given plane defined by the normal $\boldsymbol{n}$, the fatigue driving force, FP, in one loading cycle is quantified as

$$FP = \frac{\Delta\epsilon}{2}\,\sigma_{\max} + J\,\Delta\gamma\,\Delta\tau \tag{17}$$

where $\Delta\epsilon$ is the normal strain range, $\sigma_{\max}$ is the maximum normal stress, $\Delta\gamma$ is the shear strain range, $\Delta\tau$ is the shear stress range, and J is a fatigue parameter defining the importance of shear contribution to FP. At a given material point, the critical plane is detected, where FP is maximum, i.e., $\max_{\boldsymbol{n}} FP$.

In the modified Jiang–Sehitoglu criterion [31], the increase in resistance to fatigue crack initiation induced by predeformation is accounted for by allowing the dependence of the fatigue damage threshold, $\widetilde{FP}_0$, on the ratcheting strain, ϵ_{r}. Accordingly, $\widetilde{FP}_0$ is introduced as a nonlinear function of ratcheting strain and is formulated as

$$\widetilde{FP}_0\left(\epsilon_{\mathrm{r}}\right) = FP_\infty - \left(FP_\infty - FP_0\right)\exp\left(\frac{-\epsilon_{\mathrm{r}}}{\kappa}\right) \tag{18}$$

where FP_0 is the fatigue damage threshold for undeformed material, FP_∞ is the saturation value of the threshold, and κ controls how fast the threshold asymptotically approaches the saturation value with increasing deformation. The initial ratcheting strain, ϵ_{r}, in the railhead with near-surface deformed material is chosen to depend on the accumulated shear strain, γ. Accordingly, ϵ_{r} is obtained through linear interpolation of the simulation results from the predeformation tests. This procedure is similar to the method we use to obtain the material parameters and anisotropy tensors at each integration point in the railhead cross-section, as described in Section 4.1. The ratcheting strain in each predeformation simulation is computed as

$$\epsilon_{\mathrm{r}} = \sum_{i=1}^{N_{\mathrm{cycle}}}\left(\frac{\mathrm{d}\epsilon_{\mathrm{vM}}}{\mathrm{d}N}\right)_i = \sum_{i=1}^{N_{\mathrm{cycle}}}\left(\sqrt{\frac{2}{3}}\left(\left|\boldsymbol{\epsilon}^{\mathrm{dev}}(t_{\mathrm{end}})\right| - \left|\boldsymbol{\epsilon}^{\mathrm{dev}}(t_{\mathrm{start}})\right|\right)\right)_i \tag{19}$$

where N_{cycle} represents the number of cycles, $\mathrm{d}\epsilon_{\mathrm{vM}}/\mathrm{d}N$ the von Mises strain increment per loading cycle, and $\boldsymbol{\epsilon}^{\mathrm{dev}}(t_{\mathrm{start}})$ as well as $\boldsymbol{\epsilon}^{\mathrm{dev}}(t_{\mathrm{end}})$ the deviatoric strain tensors at the start and at the end of each loading cycle i. The fatigue damage increment in each loading cycle is computed as

$$\frac{\mathrm{d}D_{\mathrm{f},i}}{\mathrm{d}N} = \left(\frac{\left\langle \max_{\boldsymbol{n}} FP - \widetilde{FP}_0\right\rangle}{C_0}\right)^m \tag{20}$$

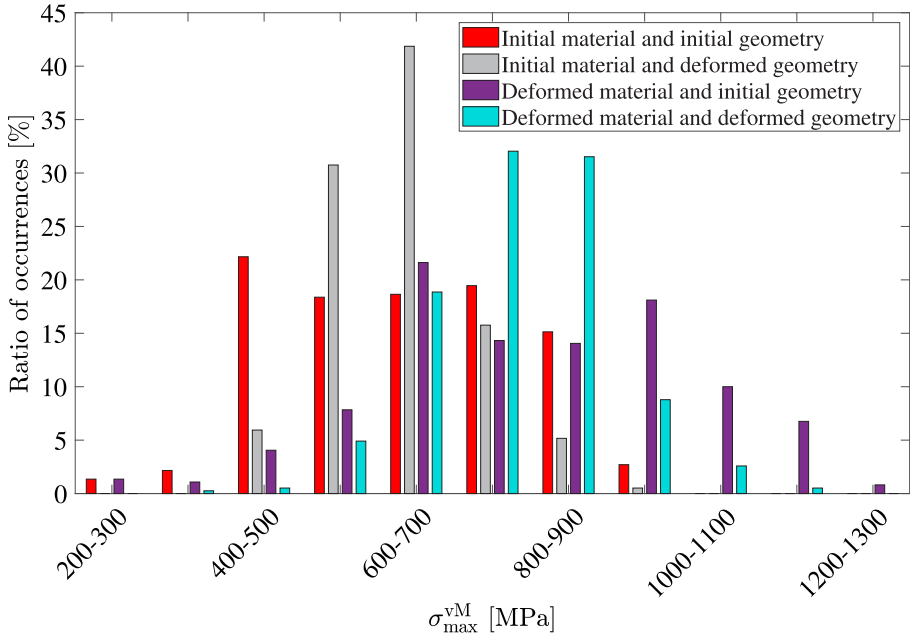

Fig. 9. Distributions of maximum von Mises stresses.

Table 4
Fatigue parameters for the modified Jiang–Sehitoglu criterion, from [31].

m [-]	C_0 [MPa]	J [-]	FP_0 [MPa]	FP_∞ [MPa]	$10^3\kappa$ [-]
2.03	98.7	0.23	0.62	2.03	9.5

where m and C_0 are fatigue parameters, and $\langle\bullet\rangle$ denotes the Macaulay bracket. In [31], the fatigue parameters for this criterion were identified for R260 pearlitic steel. Predeformation tests, proportional multiaxial LCF experiments combined with predeformation, and uniaxial high cycle fatigue tests provided calibration data. The identified fatigue parameter values are presented in Table 4.

It should be noted that, for accurate predictions of RCF crack initiation in wheel–rail contact conditions, a complete criterion accounting for the complex interaction between severe plastic deformations, wear, and RCF crack initiation is required. However, understanding the influential factors contributing to RCF damage is an essential a priori step for developing an accurate criterion. As will be shown in Section 6.2, neglecting the deformed material state and profile geometry changes leads to a significant overestimation of RCF damage.

6. Results and discussions

In this section, we present the results from the over-rolling simulations, focusing on the distribution of maximum von Mises stresses as well as accumulated plasticity, and results from RCF fatigue damage predictions in railheads. In particular, we discuss individual effects of deformed near-surface material and deformed geometry on the predictions. Following the methodology in Section 4, we have performed FE simulations of wheel over-rollings for four distinct railhead cases: (1) initial geometry with initial material (the baseline), (2) initial geometry with inhomogeneously deformed (anisotropic) material, (3) deformed geometry with initial material, and (4) deformed geometry with deformed material. The fictitious cases (2) and (3) are included to evaluate the influence of material state and rail profile geometry changes individually, before analyzing their combined effects in case (4). Initial geometry and material refer to a nominal rail profile and homogeneous virgin (isotropic) material, respectively.

6.1. Influence of material state and geometry on stress field and accumulated plasticity

Fig. 9 illustrates the distributions of the maximum von Mises stress, $\sigma^{\mathrm{vM}}_{\mathrm{max}}$, for all considered railheads and wheel passages. The results indicate that railheads with deformed material experience higher $\sigma^{\mathrm{vM}}_{\mathrm{max}}$ compared to those with initial material. Specifically, the maximum $\sigma^{\mathrm{vM}}_{\mathrm{max}}$ increases by 27% and 16% for the railheads with initial and deformed geometries, respectively. The mean values of $\sigma^{\mathrm{vM}}_{\mathrm{max}}$ are 803 MPa and 776 MPa for the geometrically initial and deformed railheads with deformed material, while they are 633 MPa and 632 MPa for the corresponding railheads with the initial material. The observed significant difference between the initial and deformed material states highlights the importance of accounting for the deformed material in the mechanical analyses of rails. In contrast, deformed geometry reduces the number of wheel passages, inducing high $\sigma^{\mathrm{vM}}_{\mathrm{max}}$. For instance, in the geometrically deformed railhead with deformed material, 12% of wheel passages result in $\sigma^{\mathrm{vM}}_{\mathrm{max}}$ higher than 900 MPa, compared to 36% for the corresponding railhead with initial geometry.

Fig. 10(a) presents accumulated plasticity in the initial geometry after the load sequence for both initial and deformed material states. When considering the deformed material, the maximum accumulated plasticity, λ, after the load sequence, decreases from 4.57 to 1.30. This implies that the deformed material decreases the accumulation rate of plasticity, even though it experiences higher $\sigma^{\mathrm{vM}}_{\mathrm{max}}$ during the wheel passages. This stems from the increased hardening slope in predeformed material states, leading to higher stresses for smaller plastic strains, see, e.g., Figs. 4(a) and 4(c). Similarly, Fig. 10(b) shows that the maximum λ decreases from 1.50 in the initial material to 0.48 in the deformed material when accounting for the deformed geometry. Since the railheads have been subjected to the mixed traffic situation described in Section 4.3, where the wheel profiles have not deformed with the rails, and to severe loading conditions, i.e., full slip with a traction coefficient of 0.4, plasticity can still occur in the railheads with highly deformed material. The impact of geometry on accumulated plasticity is also evident from the reduction in the maximum λ when transitioning from the initial to deformed geometry. For instance, the maximum λ decreases from 1.30 to 0.48 in the deformed material. This reduction is attributed to the lower frequency of load cases causing high $\sigma^{\mathrm{vM}}_{\mathrm{max}}$ in the deformed geometry compared to the initial geometry,

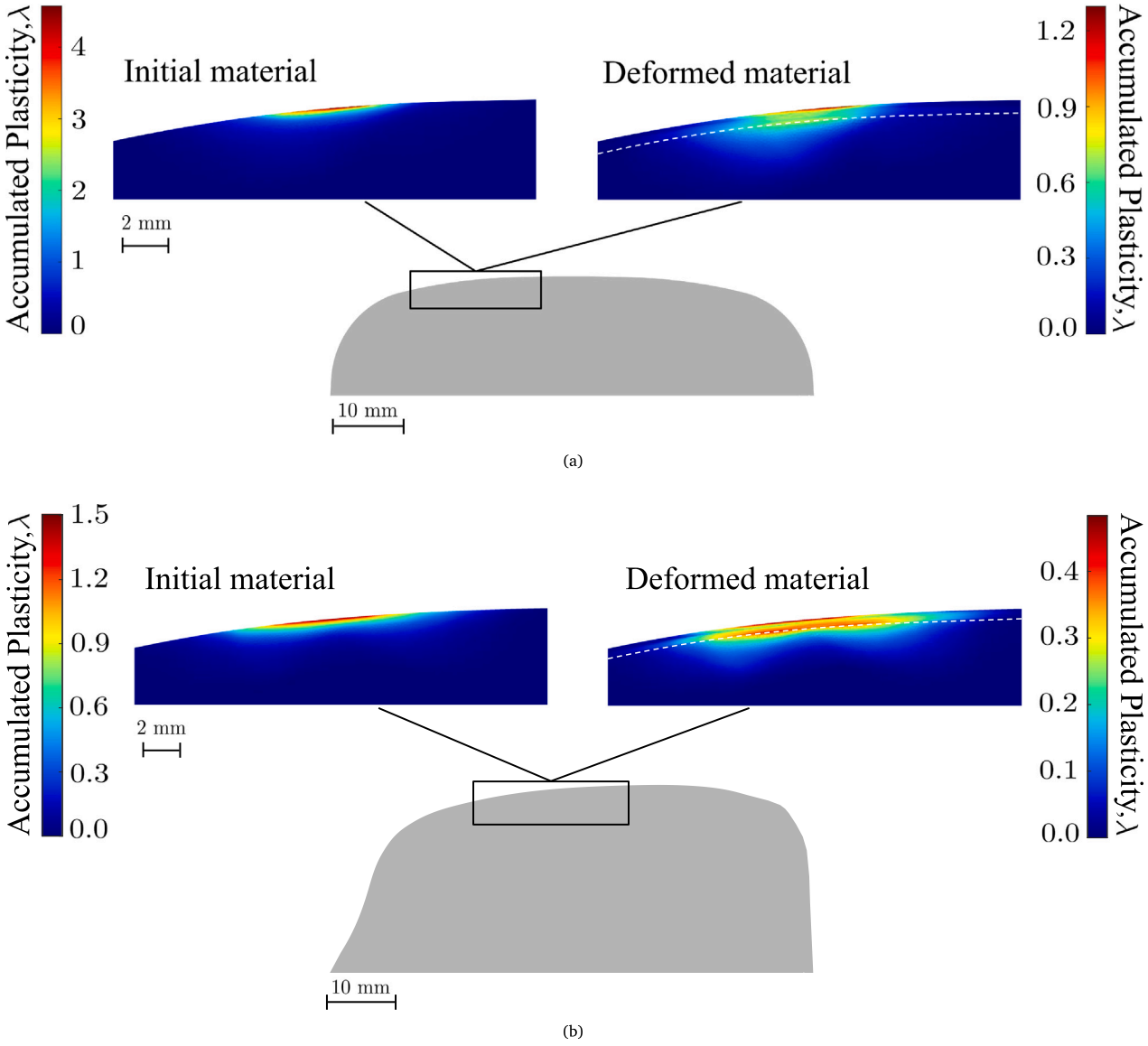

Fig. 10. Per-sequence accumulated plasticity for railheads with (a) initial and (b) deformed geometry, considering initial and deformed materials. The depth of the deformed layer is assumed to be 0.5 mm, as indicated by the dashed lines.

as previously discussed. A comparison between the baseline and the geometrically deformed railhead with deformed material shows that the combined changes in material state and geometry noticeably reduce the maximum λ, by a factor of about 10.

6.2. Influence of material state and geometry on the accumulation rate of fatigue damage

In this section, we have analyzed the influence of deformed near-surface material and deformed geometry on fatigue damage growth after the load sequence considering the previously described four railhead cases. In these analyses, we have implicitly accounted for wear through the geometrically deformed rail profile, which is based on measurements in [30]. Then, during the limited number of considered over-rollings (i.e., 348 wheel passages), we neglect the interaction between wear and surface RCF crack initiation. The deformed material is accounted for in the fatigue criterion via the spatially varying initial ratcheting strains. This variation is governed by the distribution of accumulated shear strains, as explained in Section 5.

The predicted fatigue damage growth after the load sequence for the railheads with initial geometry is presented in Fig. 11(a), where the zoomed-in views focus on the region between $x = -83$ mm and $x = -76$ mm. Accordingly, the maximum accumulated damage, D_f, in these railheads occurs where the wheel–rail contacts most often take place, see Section 4.3. The maximum D_f in the deformed material is 0.18, approximately 5 times lower than the value of 0.94 observed in the initial material. Consideration of an extreme loading condition, i.e., full slip with a high traction coefficient of 0.4, explains the reason for obtaining such high D_f values, especially in the railhead with initial material and geometry. Further, this severe loading condition, together with the mixed traffic situation, motivates why fatigue damage can still occur in the highly deformed material. The results indicate that the deformed near-surface material reduces the fatigue damage accumulation rate. Franklin et al. [51] also found that using a work-hardened coating layer on the rail surface can improve the fatigue resistance of UIC 900 A rail steel, based on twin disk experiments and field measurements.

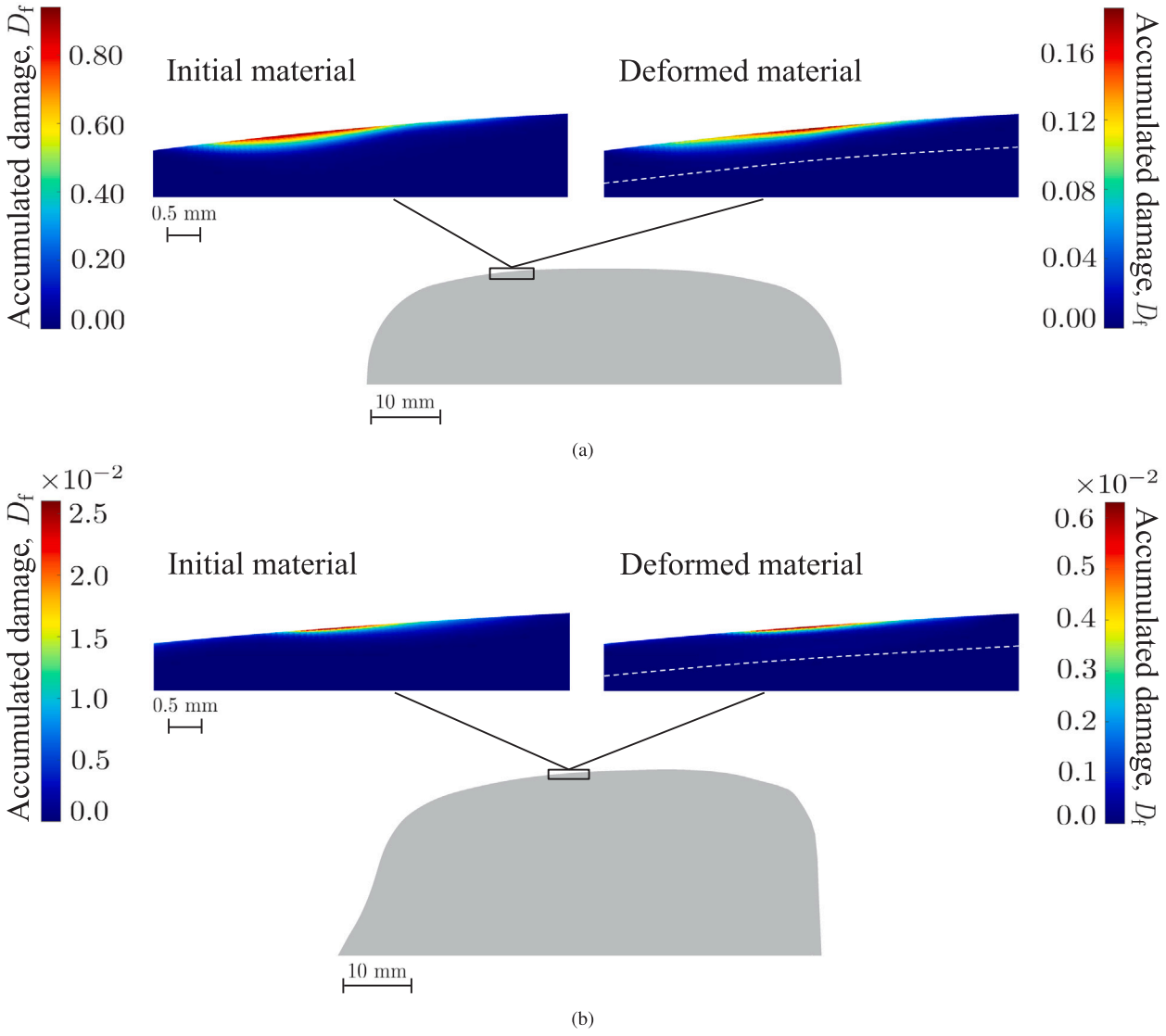

Fig. 11. Per-sequence damage growth for railheads with (a) initial and (b) deformed geometry, considering initial and deformed materials. The depth of the deformed layer is assumed to be 0.5 mm, as indicated by the dashed lines.

Referring to the geometrically deformed railheads in Fig. 11(b), the fatigue damage fields are shown for the interval between $x = -70$ mm and $x = -64$ mm, indicating that the maximum D_f occurs in the region most frequently subjected to the wheel–rail contacts. Comparable observations can be made to those seen in the railheads with initial geometry regarding the influence of deformed material. Conversely, for the same material states, the transition from the initial geometry to the deformed one drastically reduces the maximum D_f. This can also be due to the fact that the deformed geometries less frequently experience higher $\sigma_{\max}^{\mathrm{vM}}$ compared to the initial geometries. Although the deformed geometry helps reduce the maximum D_f, achieving optimal rail profile designs requires considering multiple factors to improve resistance to RCF damage [52]. Another important finding is that, when considering both deformed material and deformed geometry, the maximum D_f is reduced by a factor of approximately 150 compared to the baseline.

It can be observed that the spatial damage gradient is very large for all the studied cases and that high accumulated damage values are only obtained very close to the surface. This is illustrated in Fig. 12. Moreover, the location of the maximum D_f does not coincide with that of the maximum λ, especially in the railheads with the initial geometry. This shows the difference between the crack initiation criteria based on the maximum accumulated equivalent plastic strain, e.g. [21], and the one adopted in this paper (or the Jiang–Sehitoglu criterion [28]). The former criteria do not account for the beneficial influence of large compressive stresses, which are applied by a wheel rolling over a rail.

We also considered a lower traction coefficient of 0.3 for a railhead with initial material and geometry. The maximum accumulated damage per loading cycle still occurred at the surface, but with the noticeably lower value of 0.0049. Reducing the traction coefficient further not only decreases the maximum accumulated damage but also shifts it from the surface to the subsurface [36]. Nevertheless, we limit the scope of the paper to predictions of surface RCF crack initiation by using a high traction coefficient and investigate the influence of material state and rail profile geometry. It would be interesting to compare the fatigue damage results with those from a full-scale wheel–rail test rig experiment. However, we have instead chosen to study the case of a mixed traffic situation (which is difficult to simulate in a test rig experiment). As described in Section 4, the load sequence representing the mixed traffic consists of different wheel geometries, load amplitudes, and vehicle speeds.

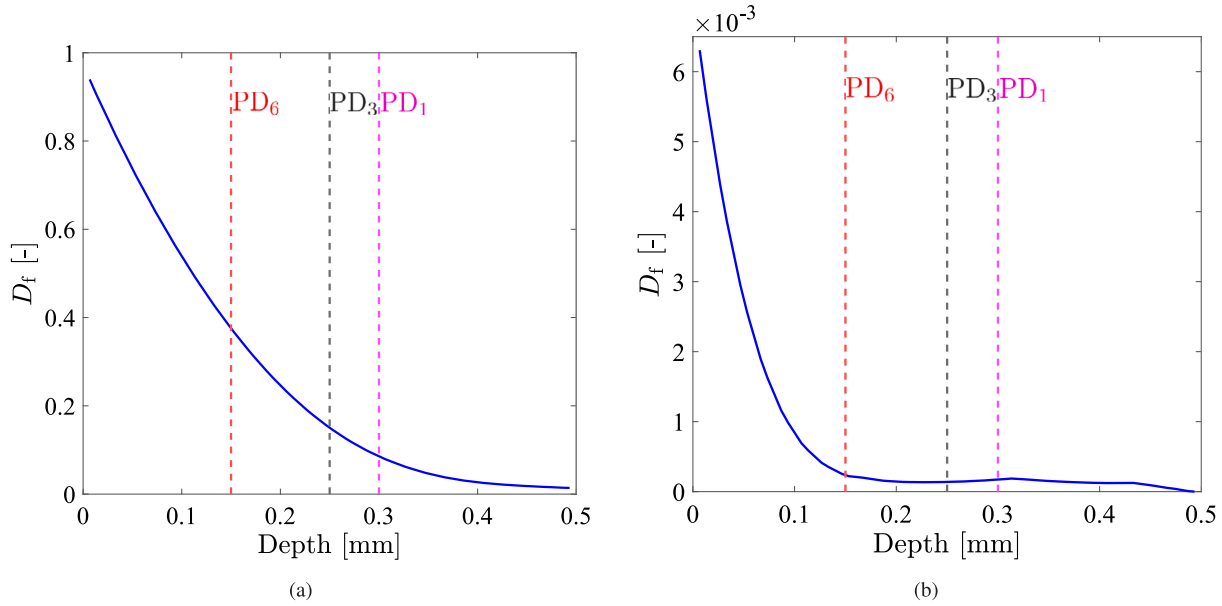

Fig. 12. Variation of accumulated damage with depth for railheads with (a) initial material and geometry and (b) deformed material and geometry. The dashed lines show the corresponding depth to each predeformation level [30].

7. Concluding remarks

In this contribution, we have investigated the influence of deformed near-surface material and deformed geometry on the mechanical and fatigue crack initiation behavior of a railhead subjected to a sequence of mixed traffic loading. An anisotropic plasticity model has been calibrated against experimental data with different amounts of accumulated shear strains, corresponding to different depths in the railhead. The identified material parameters have been used to consider spatially varying properties in the railhead. This variation is governed by the accumulated shear strain distribution, obtained from measurements in rail field samples. We have performed wheel over-rolling simulations for four railhead cases, combining either initial or deformed material with initial or deformed geometry. Finally, for RCF damage predictions, a recently developed crack initiation criterion accounting for the deformed material state has been employed.

Under full slip condition with a traction coefficient of 0.4, the results showed larger maximum von Mises stresses in the railheads with deformed material compared to those with initial material. Moreover, the deformed geometries reduced the frequency of load cases, inducing higher maximum von Mises stresses. The maximum accumulated plasticity after the considered load sequence was noticeably lower in the deformed and hardened material compared to the initial material. A similar observation applies to the railheads with deformed geometries. It was shown that the combined effect of deformed material and deformed geometry significantly decreases the maximum accumulated plasticity compared to the railhead with initial material and geometry.

Fatigue crack initiation analyses revealed that deformed near-surface material significantly reduces the rate of fatigue damage accumulation. The influence of deformed geometry in lowering the maximum accumulated damage was found to be more pronounced. Moreover, the results showed that neglecting the combined effect of deformed material and geometry leads to drastic overestimation of RCF damage. These findings show the importance of accounting for highly deformed near-surface material and rail profile geometry changes when predicting RCF damage.

CRediT authorship contribution statement

Nasrin Talebi: Writing – original draft, Visualization, Validation, Software, Methodology, Investigation, Formal analysis, Data curation, Conceptualization. **Björn Andersson:** Writing – review & editing, Visualization, Supervision, Software. **Magnus Ekh:** Writing – review & editing, Supervision, Resources, Project administration, Methodology, Funding acquisition, Conceptualization. **Knut Andreas Meyer:** Writing – review & editing, Supervision, Methodology, Data curation, Conceptualization.

Declaration of competing interest

The authors declare that they have no known competing financial interests or personal relationships that could have appeared to influence the work reported in this paper.

Acknowledgments

This work is part of the ongoing activities within the National Center of Excellence CHARMEC (www.chalmers.se/charmec). They are partially funded within the European Union's Horizon 2020 research and innovation program in the Shift2Rail project In2Track3 under grant agreement No. 101012456 and in Europe's Rail project IAM4RAIL under grant agreement No. 101101966. Caroline Ansin, from the Division of Material and Computational Mechanics, Chalmers University of Technology, is highly acknowledged for performing the multibody dynamics simulation in Simpack. The majority of the numerical simulations in this study were enabled by resources provided by the National Academic Infrastructure for Supercomputing in Sweden (NAISS) at Chalmers Center for Computational Science and Engineering (C3SE) partially funded by the Swedish Research Council through a grant agreement No. 2022-06725.

Appendix A. Closest point projection method

This section presents the adopted method to obtain the distribution of the accumulated shear strain γ in a railhead cross-section (see Fig. 2(a)). As stated in Section 2, at points P_1 and P_4, the accumulated shear strain γ is assumed to be zero at any depth η within the layer with deformed material, while, at points P_2 and P_3, we have the measured γ at certain depths, see Fig. A.13. This divides the railhead cross-section into three regions: R_1, R_2, and R_3. For a given integration point $\boldsymbol{x}_s$, the closest main node $\boldsymbol{x}_c$ and its left and right neighbors, $\boldsymbol{x}_l$ and $\boldsymbol{x}_r$ respectively, on the main surface (i.e., rail surface), are identified first.

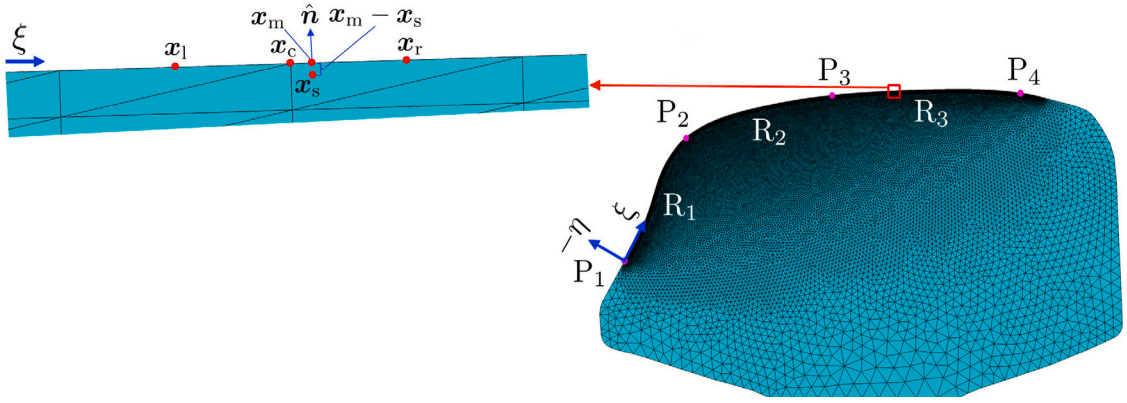

Fig. A.13. Definitions used to obtain the distribution of γ over the railhead cross-section.

Then, the closest point projection of $\boldsymbol{x}_s$ onto the main surface, $\boldsymbol{x}_m(\xi)$, is formulated as

$$\boldsymbol{x}_m(\xi) = \boldsymbol{x}_c + \xi_l\left(\boldsymbol{x}_l - \boldsymbol{x}_c\right) + \xi_r\left(\boldsymbol{x}_r - \boldsymbol{x}_c\right) \quad \text{with}$$
$$\xi_r = \max\left(0.0, \frac{\left(\boldsymbol{x}_s - \boldsymbol{x}_c\right)\cdot\left(\boldsymbol{x}_r - \boldsymbol{x}_c\right)}{\|\boldsymbol{x}_r - \boldsymbol{x}_c\|^2}\right)$$
$$\xi_l = \max\left(0.0, \frac{\left(\boldsymbol{x}_s - \boldsymbol{x}_c\right)\cdot\left(\boldsymbol{x}_l - \boldsymbol{x}_c\right)}{\|\boldsymbol{x}_l - \boldsymbol{x}_c\|^2}\right) \tag{A.1}$$

The gap function, g_s, and the depth coordinate of the integration point, η_s, are computed as

$$g_s = \left(\boldsymbol{x}_m(\xi) - \boldsymbol{x}_s\right)\cdot\hat{\boldsymbol{n}}(\xi), \quad \eta_s = |g_s| \tag{A.2}$$

where the normal vector to the master surface $\hat{\boldsymbol{n}}(\xi)$ is given by

$$\hat{\boldsymbol{n}}(\xi) = \frac{\boldsymbol{x}_m(\xi) - \boldsymbol{x}_s}{\|\boldsymbol{x}_m(\xi) - \boldsymbol{x}_s\|} \tag{A.3}$$

In the next step, whether $\boldsymbol{x}_m(\xi)$ is on the left (l) or right (r) side of $\boldsymbol{x}_c$, ξ_s is calculated through a linear interpolation scheme as follows

$$\xi_s = \xi_c + \left(\xi_i - \xi_c\right)\frac{\|\boldsymbol{x}_m(\xi) - \boldsymbol{x}_c\|}{\|\boldsymbol{x}_i - \boldsymbol{x}_c\|}, \quad i = \text{l or r} \tag{A.4}$$

where ξ_c is the corresponding coordinate of $\boldsymbol{x}_c$ in the $\xi-\eta$ coordinate system. Further, it is assumed that the shear strain γ_s at the integration point $\boldsymbol{x}_s$ follows a linear interpolation scheme and is computed as

$$\gamma_s(\xi_s, \eta_s) = \gamma_{P_j}(\eta_s) + \left(\gamma_{P_{j+1}}(\eta_s) - \gamma_{P_j}(\eta_s)\right)\frac{\xi_s - \xi_{P_j}}{\xi_{P_{j+1}} - \xi_{P_j}}, \quad j = 1, 2, \text{or } 3 \tag{A.5}$$

The index j refers to each region, R_j, depending on the value of ξ_s, and the subscript P_j refers to the location of the measured accumulated shear strains that should be used for the linear interpolation. Similarly, γ_{P_j} is calculated at η_s by linear interpolation based on the measured shear strains at different depths at the location P_j.

Appendix B. Anisotropy tensors $\hat{\mathbf{C}}$ for different predeformation levels

This section presents the anisotropy tensors, $\hat{\mathbf{C}}$, for the four predeformation levels, PD_0, PD_1, PD_3, and PD_6, obtained from the FE simulations of the predeformation tests, see Section 3.5.

• PD_0

$$\hat{\mathbf{C}} = \begin{bmatrix} 1.00 & -0.50 & -0.50 & 0.00 & 0.00 & 0.00 \\ -0.50 & 1.00 & -0.50 & 0.00 & 0.00 & 0.00 \\ -0.50 & -0.50 & 1.00 & 0.00 & 0.00 & 0.00 \\ 0.00 & 0.00 & 0.00 & 1.50 & 0.00 & 0.00 \\ 0.00 & 0.00 & 0.00 & 0.00 & 1.50 & 0.00 \\ 0.00 & 0.00 & 0.00 & 0.00 & 0.00 & 1.50 \end{bmatrix}$$

• PD_1

$$\hat{\mathbf{C}} = \begin{bmatrix} 1.83 & -0.53 & -1.30 & 0.00 & 0.00 & -0.06 \\ -0.53 & 1.06 & -0.53 & 0.00 & 0.00 & 0.11 \\ -1.30 & -0.53 & 1.83 & 0.00 & 0.00 & -0.05 \\ 0.00 & 0.00 & 0.00 & 3.12 & 0.00 & 0.00 \\ 0.00 & 0.00 & 0.00 & 0.00 & 3.12 & 0.00 \\ -0.06 & 0.11 & -0.05 & 0.00 & 0.00 & 3.00 \end{bmatrix}$$

• PD_3

$$\hat{\mathbf{C}} = \begin{bmatrix} 1.87 & -0.56 & -1.30 & 0.00 & 0.00 & -0.12 \\ -0.56 & 1.13 & -0.56 & 0.00 & 0.00 & 0.15 \\ -1.30 & -0.56 & 1.87 & 0.00 & 0.00 & -0.03 \\ 0.00 & 0.00 & 0.00 & 3.18 & 0.00 & 0.00 \\ 0.00 & 0.00 & 0.00 & 0.00 & 3.18 & 0.00 \\ -0.12 & 0.15 & -0.03 & 0.00 & 0.00 & 2.94 \end{bmatrix}$$

• PD_6

$$\hat{\mathbf{C}} = \begin{bmatrix} 1.88 & -0.62 & -1.26 & 0.00 & 0.00 & -0.17 \\ -0.62 & 1.20 & -0.58 & 0.00 & 0.00 & 0.16 \\ -1.26 & -0.58 & 1.85 & 0.00 & 0.00 & 0.02 \\ 0.00 & 0.00 & 0.00 & 3.19 & 0.00 & 0.00 \\ 0.00 & 0.00 & 0.00 & 0.00 & 3.19 & 0.00 \\ -0.17 & 0.16 & 0.02 & 0.00 & 0.00 & 2.87 \end{bmatrix}$$

Appendix C. Element thickness scaling factors for 2D GPS model

To obtain equivalent maximum von Mises stress distributions in the 2D and 3D FE simulations of train wheel roll-overs, the 2D GPS model uses scaling of the individual element thicknesses. The scaling is performed using a nominal 60E1 rail profile. A piecewise function $S(r)$, which gives different formulas for each simulated wheel passage based on the distance r from the center of the Hertzian contact pressure distribution is employed. The horizontal component of the distance r is normalized by the contact semi-axis b in the transverse direction, while the vertical component is normalized by the semi-axis a in the rail longitudinal direction. Moreover, the scaling factor $S(r)$ is defined as a linear interpolation between two values, S_i and S_{i+1}, for distance

Table C.5
Values for distance limits δ_i and scaling factors S_i of the 2D GPS model roll-over FE element thickness scaling procedure.

i	1	2	3	4
δ_i	0.5	2.0	4.0	5.0
S_i	1.0	2.0	5.0	40.0

limits δ_i and δ_{i+1} as follows:

$$S(r) = \begin{cases} S_4, & \text{if } r > \delta_4 \\ \dfrac{S_3(\delta_4 - r) + S_4(r - \delta_3)}{\delta_4 - \delta_3}, & \text{if } \delta_3 < r \le \delta_4 \\ \dfrac{S_2(\delta_3 - r) + S_3(r - \delta_2)}{\delta_3 - \delta_2}, & \text{if } \delta_2 < r \le \delta_3 \\ \dfrac{S_1(\delta_2 - r) + S_2(r - \delta_1)}{\delta_2 - \delta_1}, & \text{if } \delta_1 < r \le \delta_2 \\ S_1, & \text{if } r \le \delta_1 \end{cases} \tag{C.1}$$

The scaling factors, S_i, and corresponding distance limits δ_i are manually fitted based on stress path comparisons between the 3D and 2D roll-over simulations for the maximum von Mises stress of each over-rolling. The scaling factors, S_i, and distance limits δ_i, are presented in Table C.5.

Data availability

Data will be made available on request.

References

[1] E.E. Magel, Rolling contact fatigue: A comprehensive review, Tech. Rep., US Department of Transportation, Federal Railroad Administration, 2011, 132 p.

[2] A. Ekberg, B. Åkesson, E. Kabo, Wheel/rail rolling contact fatigue – probe, predict, prevent, Wear 314 (1) (2014) 2–12.

[3] E.E. Magel, P. Mutton, A. Ekberg, A. Kapoor, Rolling contact fatigue, wear and broken rail derailments, Wear 366–367 (2016) 249–257.

[4] F.A. Alwahdi, A. Kapoor, F.J. Franklin, Subsurface microstructural analysis and mechanical properties of pearlitic rail steels in service, Wear 302 (1–2) (2013) 1453–1460.

[5] D. Benoît, B. Salima, R. Marion, Multiscale characterization of head check initiation on rails under rolling contact fatigue: Mechanical and microstructure analysis, Wear 366–367 (2016) 383–391.

[6] B. Dylewski, M. Risbet, S. Bouvier, The tridimensional gradient of microstructure in worn rails – experimental characterization of plastic deformation accumulated by RCF, Wear 392–393 (2017) 50–59.

[7] D.F. Cannon, K. Edel, S.L. Grassie, K. Sawley, Rail defects: an overview, Fatigue Fract. Eng. Mater. Struct. 26 (10) (2003) 865–886.

[8] D.I. Fletcher, F.J. Franklin, A. Kapoor, Rail surface fatigue and wear, in: Wheel-Rail Interface Handbook, Woodhead Publishing Limited, 2009, pp. 280–310.

[9] S. Iwnicki, Handbook of Railway Vehicle Dynamics, CRC Press, 2006.

[10] R. Smallwood, J.C. Sinclair, K.J. Sawley, An optimization technique to minimize rail contact stresses, Wear 144 (1–2) (1991) 373–384.

[11] F. Wetscher, R. Stock, R. Pippan, Changes in the mechanical properties of a pearlitic steel due to large shear deformation, Mater. Sci. Eng. A 445–446 (2007) 237–243.

[12] T. Leitner, A. Hohenwarter, R. Pippan, Anisotropy in fracture and fatigue resistance of pearlitic steels and its effect on the crack path, Int. J. Fatigue 124 (2019) 528–536.

[13] A. Hohenwarter, A. Taylor, R. Stock, R. Pippan, Effect of large shear deformations on the fracture behavior of a fully pearlitic steel, Met. Mater. Trans. A Phys. Met. Mater. Sci. 42 (2011) 1609–1618.

[14] K.A. Meyer, M. Ekh, J. Ahlström, Anisotropic yield surfaces after large shear deformations in pearlitic steel, Eur. J. Mech. A Solids 82 (2020) 103977.

[15] H.P. Feigenbaum, Y.F. Dafalias, Simple model for directional distortional hardening in metal plasticity within thermodynamics, J. Eng. Mech. 134 (9) (2008) 730–738.

[16] M.P. Pietryga, I.N. Vladimirov, S. Reese, A finite deformation model for evolving flow anisotropy with distortional hardening including experimental validation, Mech. Mater. 44 (2012) 163–173.

[17] N. Larijani, G. Johansson, M. Ekh, Hybrid micro-macromechanical modeling of anisotropy evolution in pearlitic steel, Eur. J. Mech. / A Solids 38 (2013) 38–47.

[18] B. Shi, A. Bartels, J. Mosler, On the thermodynamically consistent modeling of distortional hardening: A novel generalized framework, Int. J. Plast. 63 (2014) 170–182.

[19] D. Banabic, T. Kuwabara, T. Balan, D. Comsa, D. Julean, Non-quadratic yield criterion for orthotropic sheet metals under plane-stress conditions, Int. J. Mech. Sci. 45 (5) (2003) 797–811.

[20] F. Barlat, H. Aretz, J. Yoon, M. Karabin, J. Brem, R. Dick, Linear transfomation-based anisotropic yield functions, Int. J. Plast. 21 (5) (2005) 1009–1039.

[21] A. Kapoor, A re-evaluation of the life to rupture of ductile metals by cyclic plastic strain, Fatigue Fract. Eng. Mater. Struct. 17 (2) (1994) 201–219.

[22] K. Golos, F. Ellyin, A total strain energy density theory for cumulative fatigue damage, J. Press. Vessel. Technol. Trans. ASME 110 (1) (1988) 36–41.

[23] G. Trummer, C. Marte, P. Dietmaier, C. Sommitsch, K. Six, Modeling surface rolling contact fatigue crack initiation taking severe plastic shear deformation into account, Wear 352–353 (2016) 136–145.

[24] M. Ghodrati, M. Ahmadian, R. Mirzaeifar, Modeling of rolling contact fatigue in rails at the microstructural level, Wear 406–407 (2018) 205–217.

[25] M.W. Brown, K.J. Miller, A theory for fatigue failure under multiaxial stress-strain conditions, Proc. Inst. Mech. Eng. 187 (1) (1973) 745–755.

[26] A. Ince, G. Glinka, A generalized fatigue damage parameter for multiaxial fatigue life prediction under proportional and non-proportional loadings, Int. J. Fatigue 62 (2014) 34–41.

[27] C.L. Pun, Q. Kan, P.J. Mutton, G. Kang, W. Yan, A single parameter to evaluate stress state in rail head for rolling contact fatigue analysis, Fatigue Fract. Eng. Mater. Struct. 37 (8) (2014) 909–919.

[28] Y. Jiang, H. Sehitoglu, A model for rolling contact failure, Wear 224 (1) (1999) 38–49.

[29] P. Smith, K.N., Topper, T.H., Watson, A stress-strain function for the fatigue of metals (stress-strain function for metal fatigue including mean stress effect), J. Mater. 5 (1970) 767–778.

[30] K.A. Meyer, D. Nikas, J. Ahlström, Microstructure and mechanical properties of the running band in a pearlitic rail steel: Comparison between biaxially deformed steel and field samples, Wear 396–397 (2018) 12–21.

[31] N. Talebi, J. Ahlström, M. Ekh, K.A. Meyer, Evaluations and enhancements of fatigue crack initiation criteria for steels subjected to large shear deformations, Int. J. Fatigue 182 (2024) 108227.

[32] J.W. Ringsberg, Life prediction of rolling contact fatigue crack initiation, Int. J. Fatigue 23 (7) (2001) 575–586.

[33] C. Lun, Q. Kan, P.J. Mutton, G. Kang, W. Yan, An efficient computational approach to evaluate the ratcheting performance of rail steels under cyclic rolling contact in service, Int. J. Mech. Sci. 101–102 (2015) 214–226.

[34] H. Su, C.L. Pun, P. Mutton, Q. Kan, W. Yan, Numerical study on the ratcheting performance of heavy haul rails in curved tracks, Wear 436–437 (2019) 203026.

[35] F.J. Franklin, J.E. Garnham, D.I. Fletcher, C.L. Davis, A. Kapoor, Modelling rail steel microstructure and its effect on crack initiation, Wear 265 (2008) 1332–1341.

[36] M. Ghodrati, M. Ahmadian, R. Mirzaeifar, Three-dimensional study of rolling contact fatigue using crystal plasticity and cohesive zone method, Int. J. Fatigue 128 (2019) 105208.

[37] M. Burstow, Whole Life Rail Model Application and Development–Continued Development of a Rolling Contact Fatigue Damage Parameter, Technical Report, Rail Standards and Safety Board, 2004.

[38] K.A. Meyer, A. Menzel, A distortional hardening model for finite plasticity, Int. J. Solids Struct. 232 (2021) 111055.

[39] P.J. Armstrong, C.O. Frederick, et al., A mathematical representation of the multiaxial Bauschinger effect, vol. 731, Berkeley Nuclear Laboratories Berkeley, CA, 1966.

[40] H. Burlet, G. Cailletaud, Numerical techniques for cyclic plasticity at variable temperature, Eng. Comput. 3 (2) (1986) 143–153.

[41] P. Delobelle, P. Robinet, L. Bocher, Experimental study and phenomenological modelization of ratchet under uniaxial and biaxial loading on an austenitic stainless steel, Int. J. Plast. 11 (4) (1995) 295–330.

[42] J.A. Nelder, R. Mead, A simplex method for function minimization, Comput. J. 7 (4) (1965) 308–313.

[43] K.A. Meyer, Matmodfit, 2019, https://github.com/KnutAM/matmodfi.

[44] K.A. Meyer, M. Ekh, J. Ahlström, Material model calibration against axial-torsion-pressure experiments accounting for the non-uniform stress distribution, Finite Elem. Anal. Des. 163 (2019) 1–13.

[45] Dassault Systèmes Simulia Corp., Abaqus Analysis User's Manual, two thousand twenty two th, Providence, Rhode Island, USA, 2022, Available from Dassault Systèmes.

[46] B. Andersson, M. Ekh, B.L. Josefson, Computationally efficient simulation methodology for railway repair welding: Cyclic plasticity, phase transformations and multi-phase homogenization, J. Therm. Stresses 47 (2) (2024) 164–188.

[47] B. Andersson, E. Steyn, M. Ekh, L. Josefson, Simulation-based assessment of railhead repair welding process parameters, Weld. World 69 (1) (2025) 177–197.

[48] R. Skrypnyk, M. Ekh, J.C. Nielsen, B.A. Pålsson, Prediction of plastic deformation and wear in railway crossings – comparing the performance of two rail steel grades, Wear 428–429 (2019) 302–314.

[49] R. Skrypnyk, J.C. Nielsen, M. Ekh, B.A. Pålsson, Metamodelling of wheel–rail normal contact in railway crossings with elasto-plastic material behaviour, Eng. Comput. 35 (2019) 139–155.

[50] C. Ansin, B.A. Pålsson, M. Ekh, F. Larsson, R. Larsson, Simulation and field measurements of the long-term rail surface damage due to plasticity, wear and surface rolling contact fatigue cracks in a curve, in: CM 2022 - 12th International Conference on Contact Mechanics and Wear of Rail/Wheel Systems, Conference Proceedings, 2022, pp. 591–601.

[51] F.J. Franklin, G.J. Weeda, A. Kapoor, E.J. Hiensch, Rolling contact fatigue and wear behaviour of the infrastar two-material rail, Wear 258 (7–8) (2005) 1048–1054.

[52] E.E. Magel, J. Kalousek, Designing and assessing wheel/rail profiles for improved rolling contact fatigue and wear performance, Proc. Inst. Mech. Eng. Part F: J. Rail Rapid Transit 231 (7) (2017) 805–818.